JPCCCK

AUGUST 3, 2017
VOLUME 121
NUMBER 30

pubs.acs.org/JPCC

THE JOURNAL OF PHYSICAL CHEMISTRY C

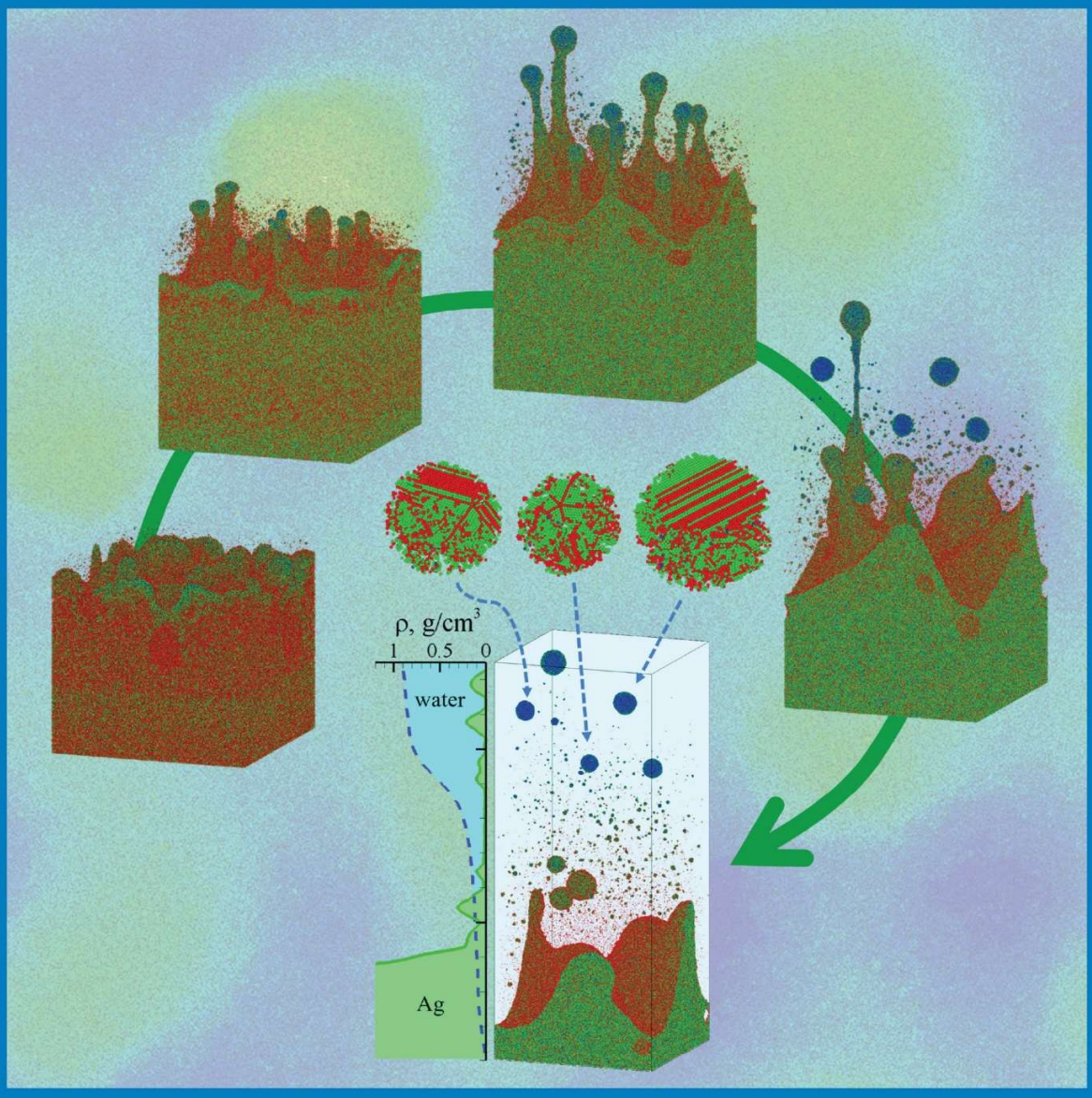

Hydrodynamic Instability and Ejection of Nanoparticles in Pulsed Laser Ablation in Liquids

ENERGY CONVERSION AND STORAGE, OPTICAL AND ELECTRONIC DEVICES, INTERFACES, NANOMATERIALS, AND HARD MATTER

ACS Publications
Most Trusted. Most Cited. Most Read.

www.acs.org

THE JOURNAL OF PHYSICAL CHEMISTRY C

Article

pubs.acs.org/JPCC

Generation of Subsurface Voids, Incubation Effect, and Formation of Nanoparticles in Short Pulse Laser Interactions with Bulk Metal Targets in Liquid: Molecular Dynamics Study

Cheng-Yu Shih, Maxim V. Shugaev, Chengping Wu, and Leonid V. Zhigilei*

Department of Materials Science and Engineering, University of Virginia, 395 McCormick Road, Charlottesville, Virginia 22904-4745, United States

Supporting Information

ABSTRACT: The ability of short pulse laser ablation in liquids to produce clean colloidal nanoparticles and unusual surface morphology has been employed in a broad range of practical applications. In this paper, we report the results of large-scale molecular dynamics simulations aimed at revealing the key processes that control the surface morphology and nanoparticle size distributions by pulsed laser ablation in liquids. The simulations of bulk Ag targets irradiated in water are performed with an advanced computational model combining a coarse-grained representation of liquid environment and an atomistic description of laser interaction with metal targets. For the irradiation conditions that correspond to the spallation regime in vacuum, the simulations predict that the water environment can prevent the complete separation of the spalled layer from the target, leading to the formation of large subsurface voids stabilized by rapid cooling and solidification. The subsequent irradiation of the laser-modified surface is found to result in a more efficient ablation and nanoparticle generation, thus suggesting the possibility of the incubation effect in multipulse laser ablation in liquids. The simulations performed at higher laser fluences that correspond to the phase explosion regime in vacuum reveal the accumulation of the ablation plume at the interface with the water environment and the formation of a hot metal layer. The water in contact with the metal layer is brought to the supercritical state and provides an environment suitable for nucleation and growth of small metal nanoparticles from metal atoms emitted from the hot metal layer. The metal layer itself has limited stability and can readily disintegrate into large (tens of nanometers) nanoparticles. The layer disintegration is facilitated by the Rayleigh−Taylor instability of the interface between the higher density metal layer decelerated by the pressure from the lighter supercritical water. The nanoparticles emerging from the layer disintegration are rapidly cooled and solidified due to the interaction with water environment, with a cooling rate of ~2×10^{12} K/s observed in the simulations. The computational prediction of two distinct mechanisms of nanoparticle formation yielding nanoparticles with different characteristic sizes provides a plausible explanation for the experimental observations of bimodal nanoparticle size distributions in laser ablation in liquids. The ultrahigh cooling and solidification rates suggest the possibility for generation of nanoparticles featuring metastable phases and highly nonequilibrium structures.

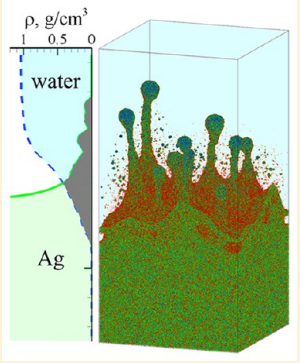

1. INTRODUCTION

Short pulse laser processing and ablation of metal targets in liquids are gaining increasing attention due to the demonstrated ability of the liquid environment to strongly affect the morphology of the laser-treated surfaces[1−11] and to enable production of clean colloidal solutions of nanoparticles.[12−17] Pulsed laser ablation in liquids (PLAL), in particular, has emerged as a promising technique featuring a number of advantages with respect to traditional chemical methods of nanoparticle generation.[18] The nanoparticles generated via PLAL are not only environmentally friendly but also chemically clean and stable.[19,20] Moreover, the ever-increasing productivity of PLAL[21−23] has attracted laboratory and industrial applications in various fields, including nanophotonics,[24] biomedicine,[25,26] and chemical catalysis.[27−29] The PLAL has also been proven to be a versatile technique capable of synthesizing nanoparticles from a board range of target material systems[30−36] and with a size control achieved through fine-tuning various experimental parameters, including the choice of the liquid medium,[36−44] control over pressure and temperature conditions in the liquid,[45−47] addition of organic ligands[13,19,48,49] or inorganic salts,[50] variation of laser irradiation parameters,[12,16,17,43] and postirradiation processing.[51−54] Moreover, the highly nonequilibrium nature of the interaction between the ablation plume and liquid environment provides opportunities for synthesis of nanoparticles with unusual structure, shape, and composition.[30,35,39,55−57]

The presence of a liquid environment not only has a profound effect on the structure and size distribution of nanoparticles generated in laser ablation but also contributes to the quenching of the transiently melted surface structures, thus creating conditions for stronger undercooling and formation of

Received: March 10, 2017
Revised: May 7, 2017
Published: June 1, 2017

DOI: 10.1021/acs.jpcc.7b02301
J. Phys. Chem. C 2017, 121, 16549−16567

highly nonequilibrium surface morphology and microstructure. While the rapid developments in the area of nanoparticle generation in PLAL[18,58,59] have overshadowed the use of the liquid environment in laser surface processing, there have been a number of experimental studies demonstrating the possibility of controlling the surface morphology through the choice of liquid and irradiation conditions.[1−11] The lack of a clear physical understanding of the mechanisms involved in liquid-assisted surface nanostructuring, however, has been hampering the transition from the initial demonstration of promising results for specific material systems to the emergence of a robust general technique of surface processing.

In order to fully utilize the potential of pulsed laser irradiation in liquids for both surface nanostructuring and generation of nanoparticles with well-controlled structure, composition, and size distribution, one needs to improve the understanding of the laser-induced processes responsible for the generation of frozen surface features and colloidal nanoparticles. Such an understanding can only emerge from simultaneous progress in time-resolved experimental probing, theoretical description, and computational modeling of laser-induced processes.

Experimentally, the information on the expansion of a bubble generated due to the interaction of the ablation plume with liquid environment[60−62] has recently been complemented by the results of small-angle X-ray scattering (SAXS) probing of the evolution of the nanoparticle size distribution with respect to time and position inside the bubble.[63−66] The experimental evidence suggests that the cavitation bubble serves as a reaction chamber for the nanoparticle nucleation, growth, coalescence, and solidification, while two or more distinct nanoparticle populations may appear at different stages of the bubble expansion and collapse. The initial and most critical stage of the nanoparticle formation at the early stage of the bubble generation and expansion, however, remains beyond the temporal and spatial resolution of the experimental techniques. Moreover, the evaluation of thermodynamic states of the ablation plume confined in the cavitation bubble based on the dynamics of the bubble expansion[60−62] can only be done with a large degree of uncertainty.

The theoretical and computational treatments of laser−material interactions in liquids have also been hampered by the highly nonequilibrium nature of the laser-induced processes. The interaction of the ablation plume with liquid environment adds an additional layer of complexity to the laser ablation, which by itself is a rather complex phenomenon. The continuum-level modeling, in particular, while successful in providing initial insights into the effect of the spatial confinement on the ablation plume expansion and phase decomposition,[67,68] has been suffering from the lack of an adequate description of some of the key processes, such as vaporization of the liquid, mixing of the ablation plume with liquid environment, and generation of nanoparticles in the mixing region. The atomic-level molecular dynamics (MD) computational technique is suitable for exploring nonequilibrium phenomena and can provide atomic-level insights into the laser-induced processes, as reviewed in refs 69−71. The added cost of the atomistic representation of the liquid environment, combined with the relatively large time and length scales of processes responsible for the nanoparticle generation in PLAL and/or resolidification of the irradiated surfaces, however, have been preventing applications of MD simulations to the analysis of laser-induced surface nanostructuring and nanoparticle generation in liquids.

New opportunities for expanding the domain of applicability of MD simulations have been provided by recent developments of a computationally efficient coarse-grained representation of liquid environment[72−74] and advanced boundary conditions,[75] which have led to the design of a hybrid atomistic−coarse-grained MD model capable of revealing the specific characteristics of laser−material interactions in liquids.[74,76] In particular, simulations of laser ablation of thin metal films in water environment have predicted the existence of two distinct mechanisms of the nanoparticle formation in PLAL during the first nanoseconds of the ablation process, the nucleation and growth of small nanoparticles in the metal−water mixing region, and generation of larger (tens of nanometers) nanoparticles through the breakup of a hot molten metal layer formed at the front of the expanding ablation plume confined by the water environment.[74] The latter mechanism is activated by the development of the Rayleigh−Taylor instability at the interface between the metal layer and water brought to the supercritical state by the interaction with the hot ablation plume. First simulations of laser melting and resolidification of bulk metal targets in liquids have also been performed and suggested that the presence of a liquid environment suppresses nucleation of subsurface voids, provides an additional pathway for cooling through the heat conduction to the liquid, and facilitates the formation of nanocrystalline surface structure.[76] In the simulations reported in this paper, we extend the investigation of laser interactions with bulk metal targets to higher laser fluences, where spallation or phase explosion of a surface region of the irradiated target in vacuum takes place. The implications of the interaction of the ablation plume with liquid environment on the formation of nanoparticles and morphology of resolidified surface are analyzed based on the simulation results.

The paper is organized as follows. A brief description of the computational model and parameters of the computational setup is provided in Section 2. The results of large-scale simulations of laser spallation and phase explosion confined by the liquid environment are reported in Sections 3.1 and 3.2. The implications of Rayleigh−Taylor instability at the plume−water interface for the nanoparticle generation are discussed in Section 3.3. The results of the second pulse laser irradiation of a target already modified by the first pulse as well as the general microscopic mechanisms of nanoparticle generation in the regime of confined phase explosion are presented in Section 3.4. A summary of the computational predictions is provided in Section 4.

2. COMPUTATIONAL MODEL FOR MD SIMULATION OF LASER INTERACTIONS WITH METALS IN LIQUIDS

The simulations reported in this paper are performed with a hybrid computational model combining a coarse-grained representation of liquid, a fully atomistic description of laser interaction with metal targets, and acoustic impedance matching boundary conditions designed to mimic the non-reflecting propagation of the laser-induced pressure waves through the boundaries of the computational domain. A schematic representation of the computational system is shown in Figure 1. The computational setup is designed and parametrized for a bulk Ag target covered by water and irradiated by femtosecond and picosecond laser pulses. A brief

DOI: 10.1021/acs.jpcc.7b02301
J. Phys. Chem. C 2017, 121, 16549−16567

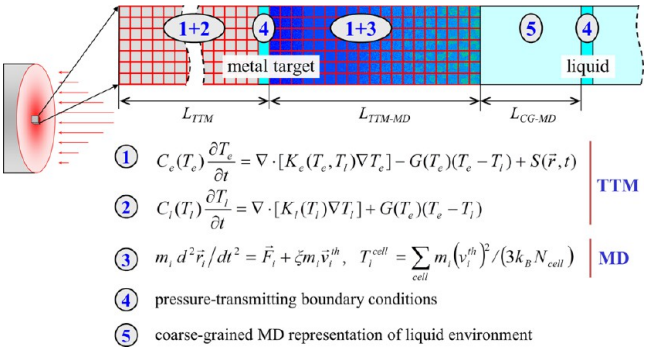

Figure 1. Schematic representation of the combined continuum—coarse-grained—atomistic model for simulation of laser interactions with metals in the liquid environment. The top part of the metal target is represented by the TTM-MD model described in Section 2.1; the temperature evolution in the deeper part of the target is described by TTM equations; and part of the liquid environment adjacent to the metal surface is simulated with a coarse-grained MD model described in Section 2.3. At the bottom of the TTM-MD and on the top of the coarse-grained MD regions, the pressure wave transmitting boundary conditions are imposed. Both the Ag target and the liquid overlayer are assumed to be sufficiently thick to ensure that any effects caused by the reflection of the laser-induced pressure waves from the outer surfaces of the target and overlayer can be neglected. The computational system represents a small region within the laser spot, and periodic boundary conditions are applied in the lateral directions, parallel to the surface of the target. The spatial discretization in the continuum part of the model and the dimensions of the atomistic and continuum regions are not drawn to scale.

description of the main components of the computational model as well as details of the computational setup are provided below.

2.1. TTM-MD Model for Laser Interactions with Metals. The laser interaction with bulk metal target is simulated with a hybrid atomistic-continuum model[77−81] that combines the classical molecular dynamics (MD) method with the two-temperature model (TTM)[82] commonly used in the simulations of short pulse laser interactions with metals, e.g., refs 83−85. The idea of the combined TTM-MD model is schematically illustrated in Figure 1 and is briefly explained below.

In the original TTM, the time evolution of the lattice and electron temperatures, T_l and T_e, is described by two coupled differential equations (eqs 1 and 2 in Figure 1) that account for the electron heat conduction in the metal target and the energy exchange between the electrons and atomic vibrations. In the combined TTM-MD method (eqs 1 and 3 in Figure 1), MD substitutes the TTM equation for the lattice temperature in the surface region of the target, where laser-induced structural and phase transformations take place. The diffusion equation for the electron temperature, T_e, is solved by a finite difference method simultaneously with MD integration of the equations of motion of atoms. The cells in the finite difference discretization are related to the corresponding volumes of the MD system, and the local lattice temperature, T_l^{cell}, is defined for each cell from the average kinetic energy of thermal motion of atoms (N_{cell} is the instantaneous number of atoms in a given cell). Note that, following the terminology established in the literature presenting TTM calculations, the term "lattice temperature" does not imply the preservation of the crystalline order in the irradiated material but is simply used here to refer to the temperature of the ionic subsystem that is brought out of equilibrium with the conduction-band electrons.

The electron temperature enters a coupling term, $\xi m_i \vec{v}_i^{th}$, that is added to the MD equations of motion to account for the energy exchange between the electrons and atomic vibrations. In this coupling term, ξ is a coefficient that depends on the instantaneous difference between the local lattice and electron temperatures as well as the strength of the electron−phonon coupling;[77] m_i is the mass of an atom i; $\vec{v}_i^{th}$ is the thermal velocity of the atom defined as $\vec{v}_i^{th} = \vec{v}_i - \vec{v}^c$, where $\vec{v}_i$ is the actual velocity of atom i; and $\vec{v}^c$ is the velocity of the center of mass of a cell to which the atom i belongs. The expansion, density variation, and, at higher fluences, disintegration of the irradiated target predicted in the MD part of the model are accounted for through the corresponding changes of the parameters of the TTM equation for electron temperature. The atoms crossing from one cell to another carry the corresponding electron thermal energy along, thus ensuring the total energy conservation.[86] The three-dimensional solution of the diffusion equation for T_e is used in large-scale simulations of laser spallation and ablation,[79−81] where the dynamic material decomposition may result in lateral density and temperature variations, as well as in simulations of spatially localized laser energy deposition.[87−89]

As schematically illustrated in Figure 1, the atomic-level TTM-MD representation is used only for the top part of the metal target, where the laser-induced structural modifications take place. In the deeper part of the target, beyond the TTM-MD region, the electron heat conduction and the energy exchange between the electrons and the lattice are described by the conventional TTM equations, with L_{TTM} chosen to ensure negligible temperature changes at the bottom of the computational domain during the simulation time. A dynamic pressure-transmitting boundary condition[75,90,91] is applied at the bottom of the MD part of the system (marked as ④ in Figure 1) to ensure nonreflecting propagation of the laser-induced stress wave from the MD region of the computational system to the bulk of the target. The energy carried away by the stress wave is calculated, so that the total energy conservation in the combined model could be monitored in the course of the simulation.[92]

2.2. Interatomic Potential and TTM Parameters for Ag. The interatomic interactions in the MD part of the model are described by the embedded atom method (EAM) potential with the functional form and parametrization developed in ref 93. A cutoff function suggested in ref 94 is added to the potential to smoothly bring the interaction energies and forces to zero at interatomic distance of 5.5 Å. Although the potential is fitted to low-temperature values of the equilibrium lattice constant, sublimation energy, elastic constants, and vacancy formation energy, it also provides a good description of high-temperature thermodynamic properties of Ag[95] relevant to the simulation of laser-induced processes. In particular, the equilibrium melting temperature, T_m, determined in liquid−crystal coexistence simulations, is 1139 ± 2 K,[96] about 8% below the experimental values of 1235 K.[97] The threshold temperature for the onset of the explosive phase separation into liquid and vapor, T^*, determined in simulations of slow heating of a metastable liquid, is found to be ~3450 K at zero pressure and ~4850 K at 0.5 GPa.[75] The onset of the phase explosion can be expected at about 10% below the critical temperature,[98−100] and the values of T^* calculated for the EAM Ag material are not in conflict with the range of experimental

DOI: 10.1021/acs.jpcc.7b02301
J. Phys. Chem. C 2017, 121, 16549−16567

values of the critical temperature of Ag spanning from 4300 to 7500 K.[101]

The electron temperature dependences of the thermophysical material properties included in the TTM equation for the electron temperature (electron−phonon coupling factor and electron heat capacity) are taken in the forms that account for the thermal excitation from the electron states below the Fermi level.[102] The electron thermal conductivity is described by the Drude model relationship, $K_e(T_e,T_l) = v^2C_e(T_e)\tau_e(T_e,T_l)/3$, where $C_e(T_e)$ is the electron heat capacity; v^2 is the mean square velocity of the electrons contributing to the electron heat conductivity, approximated in this work as the Fermi velocity squared, v_F^2; and $\tau_e(T_e,T_l)$ is the total electron scattering time defined by the electron−electron and electron−phonon scattering rates, $1/\tau_e = 1/\tau_{e-e} + 1/\tau_{e-ph} = AT_e^2 + BT_l$. The value of the coefficient A, 3.57×10^6 s^{-1} K^{-2}, is estimated within the free electron model,[96] following the approach suggested in ref 103. The value of the coefficient B, 1.12×10^{11} s^{-1} K^{-1}, is fitted to the experimental thermal conductivity of solid Ag at the melting temperature, 363 W m^{-1} K^{-1}.[104]

2.3. Coarse-Grained MD Representation of Liquid Environment. The direct application of the conventional all-atom MD representation of liquids in large-scale simulations of laser processing or ablation is not feasible due to the high computational cost. Thus, a coarse-grained representation of the liquid environment, where each particle represents several molecules, is adapted in this work. The coarse-grained MD model combines the breathing sphere model developed for simulations of laser interaction with molecular systems[105,106] with a heat bath approach that associates an internal energy variable with each coarse-grained particle.[72−74,107,108] The heat bath approach makes it possible to account for the degrees of freedom that are missing in the coarse-grained model and to reproduce the experimental heat capacity of the liquid.[72] The energy exchange between the internal heat bath energy of the particles and their dynamic degrees of freedom is controlled by the dynamic coupling between the translational degrees of freedom and the vibrational (breathing) mode associated with each coarse-grained particle (the particles are allowed to change their radii or to "breath"). The breathing mode is, in turn, directly connected to the internal heat bath through a damping force applied to the breathing motion and proportional to the difference between the local temperature associated with the breathing motion and the temperature of the heat bath.[72−74] The coupling between the heat bath and the breathing mode is done at the level of individual coarse-grained particles, and the capacity of the heat bath is chosen to reproduce the real heat capacity of the group of atoms represented by each coarse-grained particle. Effectively, the breathing mode serves as a "gate" for accessing the energy stored in the heat bath and controlling the energy exchange between the heat bath and the energy of translational motion of the particles.

In the parametrization of the coarse-grained model for water, each particle has a mass of 50 Da and represents about three real water molecules. The potential describing the interparticle interactions is provided in ref 72, and the parameters of the potential are selected to ensure a satisfactory semiquantitative description of experimental properties of water. In particular, the density and heat capacity are directly fitted to the experimental values, while the speed of sound, bulk modulus, viscosity, surface energy, melting temperature, critical temperature, and critical density do not deviate from the experimental values by more than 25%.[74]

As shown in Figure 1, the coarse-grained MD representation of the water environment is used only in a layer with thickness of $L_{CG\text{-}MD}$ adjacent to the surface of the metal target. The thickness of this layer is chosen to include the region affected by the phase transformations induced in water by the interaction with hot metal surface and ablation plume. At the top of the coarse-grained MD region, a dynamic acoustic impedance matching boundary condition based on an imaginary plane approach[75] is applied to ensure nonreflective propagation of the pressure wave generated at the metal−water interface into the bulk of a thick water overlayer. This boundary condition is suitable for reproducing experimental conditions where the reflection of the pressure wave from the outer surface of the water overlayer does not have any significant effect on processes occurring in the vicinity of the irradiated metal surface.

The interactions between Ag atoms and the coarse-grained water particles are described by the Lennard-Jones (LJ) potential fitted to match the diffusion of metal atoms and small clusters in water predicted by the Stoke−Einstein equation at 300 K.[74] Furthermore, the parameters of the LJ potential are chosen to ensure that the values of the equilibrium O−Ag distance and the adsorption energy of water on a Ag surface predicted in *ab initio* simulations[109−112] are roughly reproduced by the coarse-grained model. Note that, while it is possible to incorporate the description of chemical reactions into the framework of the coarse-grained MD model,[106,113,114] we have not included descriptions of oxidation or other chemical reactions in the version of the model used in the present study.

2.4. Computational Setup and Simulation Parameters. The simulations are performed for a Ag bulk target covered by water, as shown in Figure 1. The initial target has fcc crystal structure and (001) orientation of the free surface. The periodic boundary conditions are applied in the lateral directions, parallel to the surface of the target. The dimensions of the computational system in the lateral directions are 98.7 nm × 98.7 nm. The depth of the surface part of the Ag target represented with atomistic resolution, $L_{TTM\text{-}MD}$ in Figure 1, and the corresponding number of Ag atoms are different in simulations performed at different absorbed laser fluences, namely, $L_{TTM\text{-}MD}$ = 200 nm (112 million Ag atoms) at F_{abs} = 150 mJ/cm^2 in Section 3.1, $L_{TTM\text{-}MD}$ = 400 nm (224 million Ag atoms) at F_{abs} = 400 mJ/cm^2 in Section 3.2, and $L_{TTM\text{-}MD}$ = 280 nm (126 million Ag atoms) at F_{abs} = 300 mJ/cm^2 in Section 3.4. The thickness of the part of the water overlayer represented by the coarse-grained MD model discussed in Section 2.3 is the same in the three simulations, $L_{CG\text{-}MD}$ = 300 nm, which corresponds to 34 million coarse-grained particles. The size of the TTM part of the system, L_{TTM} in Figure 1, is 3 μm, 2.8 μm, and 2.9 μm in the simulations discussed in Sections 3.1, 3.2, and 3.4, respectively. The thicknesses of the parts of the system represented with atomic and molecular resolutions, $L_{TTM\text{-}MD}$ and $L_{CG\text{-}MD}$, are chosen based on the results of back-of-the-envelope estimations of zones affected by the laser-induced phase transformations, followed by small-scale test simulations performed for systems with lateral dimensions of 5 nm × 5 nm. In order to highlight the effect of the liquid environment on the laser-induced processes, the simulations described in Sections 3.1 and 3.2 are also performed in vacuum, i.e., without the

DOI: 10.1021/acs.jpcc.7b02301
J. Phys. Chem. C 2017, 121, 16549−16567

liquid overlayer but with otherwise identical computational setups and irradiation conditions.

The laser irradiation of the target is represented in the model through a source term added to the TTM equation for the electron temperature.[77] The source term describes excitation of the conduction band electrons by a laser pulse with a Gaussian temporal profile and reproduces the exponential attenuation of laser intensity with the depth under the surface. The optical absorption depth, 12 nm at laser wavelength of 800 nm,[115] combined with the effective depth of the "ballistic" energy transport, estimated to be about 56 nm for Ag,[75,80] is used in the source term of the TTM equation.[77,83] The laser pulse durations, τ_L, defined as full width at half-maximum of the Gaussian profile, is 100 fs in all simulations. The reflectivity of the surface is not defined in the model since the absorbed laser fluence, F_{abs}, rather than the incident fluence is used in the presentation of the simulation results.

All systems are equilibrated at 300 K for 300 ps before applying laser irradiation. The simulations are performed with a computationally efficient parallel code implementing the combined TTM-MD—coarse-grained MD model, with a three-dimensional treatment of the electronic heat conduction in the TTM-MD part of the computational system.

The implementation of the model used in this work does not account for ionization of the ejected plume, as simple estimations based on the Saha–Eggert equation[116,117] suggest that the degree of ionization in the ablation plume is negligible under irradiation conditions applied in the simulations reported in this paper. As a result, the nanoparticle formation through nucleation around ion seeds in "misty plasma" considered for high fluence nanosecond PLAL[61,118] is not relevant to the milder irradiation conditions and short pulses considered in the present work.

3. RESULTS AND DISCUSSION

The results of large-scale simulations of laser interactions with a Ag target in the spallation and phase explosion irradiation regimes are presented first, in Sections 3.1 and 3.2. The nature of the Rayleigh–Taylor instability developing at the interface between the ablation plume and the water environment and responsible for the generation of large nanoparticles is discussed in Section 3.3. This discussion is followed in Section 3.4 by the results of a simulation mimicking the effect of the second pulse irradiation of a target modified by prior irradiation and providing insights into the incubation effect and the mechanisms of the nanoparticle generation at the initial stage of the ablation process.

3.1. Generation of Subsurface Voids through Partial Spallation in Liquid. The simulations discussed in this section are performed for irradiation conditions that correspond to the regime of photomechanical spallation, when the dynamic relaxation of laser-induced stresses results in subsurface cavitation and ejection of molten layers or large droplets from the irradiated target.[79,119−121] In particular, for the pulse duration of τ_L = 100 fs, the absorbed fluence applied in the simulations, F_{abs} = 150 mJ/cm^2, is about 50% above the spallation threshold in vacuum.[75,80,81] The visual picture of the spallation process in vacuum is shown in Figure 2. A large number of small subsurface voids can be seen to appear in the molten part of the target by the time of 100 ps. The voids are generated in a region where the strength of the unloading tensile wave produced due to the interaction of the laser-induced compressive stresses with the free surface of the

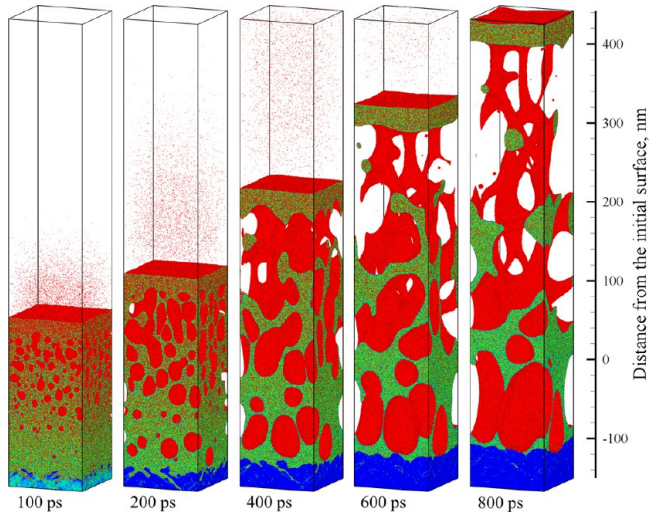

Figure 2. Snapshots of atomic configurations predicted in a simulation of laser spallation of a bulk Ag target irradiated *in vacuum* by a 100 fs laser pulse at an absorbed fluence of 150 mJ/cm^2. Only a part of the computational system from −150 to 443 nm with respect to the initial surface of the target is shown in the snapshots. The atoms are colored according to their potential energies, with the scale chosen so that the crystalline part of the target is blue, liquid Ag is green, and the top surface, internal surfaces of the voids, and vapor-phase Ag atoms are red.

irradiated target exceeds the limit of the dynamic stability of the metastable liquid against the onset of the cavitation.[79] The growth, coalescence, and percolation of the voids result in the formation of a complex foamy structure of interconnected liquid regions connecting the bulk of the target with an ∼28 nm thick top liquid layer moving away from the target with an almost constant velocity of ∼530 m/s (Figures 2 and 4a). The foamy structure coarsens with time and eventually decomposes into individual droplets on the time scale of nanoseconds. The top liquid layer is also expected to lose stability and decompose into large droplets, estimated to have diameters from hundreds of nanometers to tens of micrometers.[79]

The presence of a water environment has a profound effect on the dynamics of the spallation process, as can be seen from snapshots and the density contour plot shown in Figures 3 and 4b. While the multiple voids are still generated in a subsurface region of the target, partial propagation of the laser-induced pressure wave into the water overlayer reduces the strength of the unloading tensile wave and increases the thickness of the molten layer that is not affected by the void nucleation. Moreover, the resistance of the water environment to the outward motion of the surface layer decelerates the layer and, at about 1.35 ns after the laser pulse, reverses the direction of its motion back toward the target. The deceleration of the top layer under the water confinement makes it possible for the material that forms the expanding foamy structure in vacuum (Figure 2) to join the top layer, resulting in a substantial thickening of the layer (Figures 3 and 4b). This general picture of the spallation confined by a liquid environment is consistent with the results of earlier one-dimensional hydrodynamic simulations,[67] where the deceleration of the top spalled layer followed by merging of several spalled layers is predicted for femtosecond laser irradiation of a Au target in water.

The resistance of the water environment to the outward motion of the top molten layer not only slows down the layer

DOI: 10.1021/acs.jpcc.7b02301
J. Phys. Chem. C 2017, 121, 16549−16567

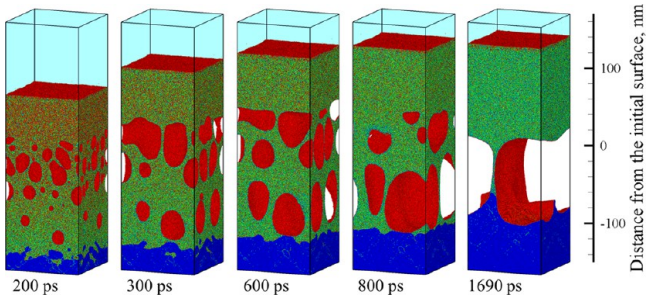

Figure 3. Snapshots of atomic configurations predicted in a simulation of an incomplete laser spallation of a bulk silver target irradiated *in water* by a 100 fs laser pulse at an absorbed fluence of 150 mJ/cm^2. Only a part of the computational system from −150 to 170 nm with respect to the initial surface of the Ag target is shown in the snapshots. The atoms are colored according to their potential energies: from blue for the crystalline part of the target, to green for liquid Ag, and to red for internal surfaces of the voids and water−Ag interface. The molecules representing the water environment are blanked, and the presence of water is illustrated schematically by a light blue region above the Ag target.

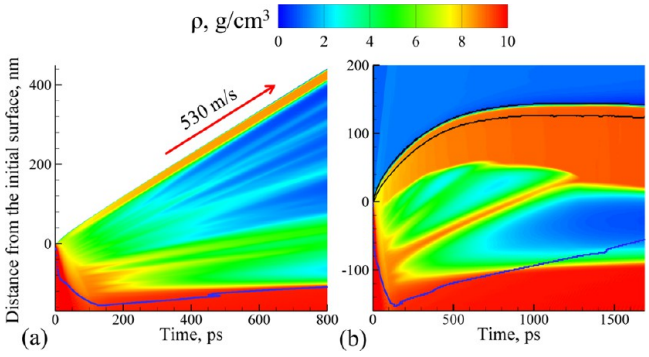

Figure 4. Density contour plots predicted in simulations of laser spallation of a bulk Ag target irradiated by a 100 fs laser pulse at an absorbed fluence of 150 mJ/cm^2 in vacuum (a) and in water (b). The blue line shows the location of the melting and solidification fronts. In (b), the two black lines outline the water−Ag mixing region defined as a region where both water molecules and Ag atoms are present. Snapshots from the simulations are shown in Figures 2 and 3.

but also prevents its complete separation from the target. The conductive cooling through the remaining liquid bridge connecting the top layer to the bulk of the target, combined with an additional cooling due to the interaction with the water environment, brings the average temperature of the liquid layer down to the melting point of the EAM Ag, T_m = 1139 K,[96] by the time of 740 ps and undercools the layer down to ∼0.85 T_m by the end of the simulation at 1690 ps. The cooling of the molten layer is illustrated by Figure 5, where the average temperature of the top 10 nm thick part of the layer is plotted. To save computational time, the simulation was not continued beyond 1690 ps. Nevertheless, one can estimate, based on the cooling rate, the solidification front advancement, and the downward velocity of the top liquid layer, that the layer would solidify well before it could redeposit to the substrate. The solidification is expected to mostly proceed by the epitaxial regrowth of the single-crystal target through the bridge into the top layer, with a possible additional contribution from the homogeneous nucleation of new crystallites in the strongly undercooled liquid layer. At the end of the simulation, the front of the epitaxial solidification is already passing through the

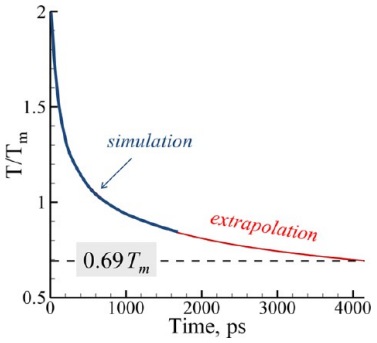

Figure 5. Evolution of the average temperature of a 10 nm thick top surface layer of a Ag target irradiated in water by a 100 fs laser pulse at an absorbed fluence of 150 mJ/cm^2. The part of the curve colored blue is the data obtained in the simulation, while the part colored in red is the extrapolation beyond the time of the simulation. The snapshots and density contour plot from the simulation are shown in Figures 3 and 4b, respectively.

bridge, as can be seen from the last snapshot shown for 1690 ps in Figure 3 as well as from the contour plot in Figure 4b, where the advancement of the solidification front is shown by the blue line. As has been demonstrated in earlier studies,[80,81] a massive homogeneous nucleation of new crystallites can be expected when the temperature the EAM Ag material drops down to ∼0.69 T_m. Using an extrapolation of the cooling curve in Figure 5, one can estimate that this level of undercooling should be reached by ∼4 ns, which sets the upper limit for the time needed for the complete resolidification of the target.

The computational prediction of the formation of large subsurface voids stabilized by the rapid cooling and solidification of the surface region has two important implications. First, the subsurface voids generated by the laser spallation confined by water are many times larger than the ones observed in simulations performed close to the spallation threshold in vacuum,[80] thus suggesting a strong effect of liquid environment on modification of surface morphology and microstructure. Second, the formation of a complex foamy structure of frozen walls and bridges connecting a thin surface layer to the bulk of the target can be expected to have a strong impact on the generation of nanoparticles in the multipulse irradiation regime. The latter implication is considered in more detail in Section 3.4, where the results of a simulation of the second pulse irradiation of a target modified by the first pulse are discussed. The implication of the surface morphology is discussed below, in the remainder of this section.

While the subsurface cavitation and surface swelling produced by trapping of laser-generated voids by the solidification front has been observed in both simulations and experiments performed in vacuum,[80,122−125] the laser fluences resulting in the formation of subsurface voids cover a rather narrow range in the vicinity of the spallation threshold. For example, a recent atomistic simulation study of surface swelling of a Ag target irradiated in vacuum[80] shows the formation of subsurface voids and corresponding swelling of the surface by ∼17 nm at an absorbed laser fluence of 85 mJ/cm^2. An increase of the fluence to 90 mJ/cm^2 leads to the separation/spallation of the layer and generation of frozen surface nanospikes rather than subsurface voids.[81] In contrast, the irradiation of a Ag target in the water environment at an almost twice higher laser fluence, 150 mJ/cm^2, does not lead to the complete separation of the top layer. The solidification of the surface region in this

DOI: 10.1021/acs.jpcc.7b02301
J. Phys. Chem. C 2017, 121, 16549−16567

case can be expected to produce much larger subsurface voids and the corresponding swelling of the irradiated area (Figure 4b).

Similar to the subsurface voids observed in simulations performed in vacuum, the voids and the large surface expansion produced in the simulation illustrated by Figures 3 and 4b are driven by the relaxation of laser-induced stresses and can be described as incomplete spallation. This is apparent from Figure 6a,b, where the evolution of the number and total

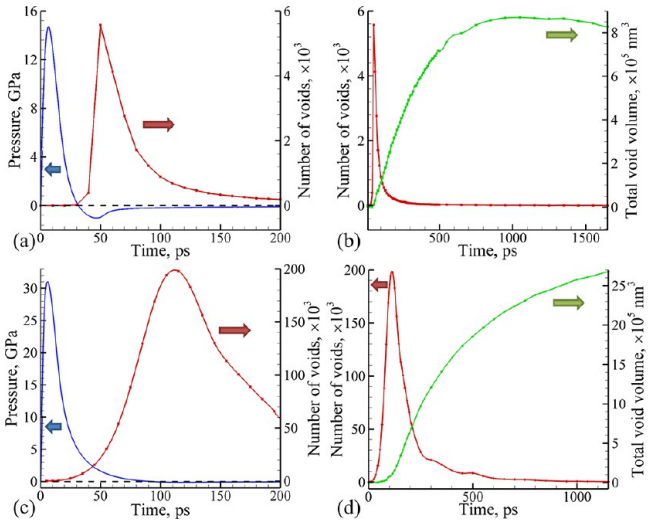

Figure 6. Evolution of pressure (blue curves in a and c), the total number of voids (red curves), and the total volume of all voids (green curves in b and d) predicted in simulations of Ag targets irradiated in water by 100 fs laser pulses at absorbed fluences of 150 mJ/cm^2 (a,b) and 400 mJ/cm^2 (c,d). The pressure is averaged over a region between 10 and 60 nm under the initial surface of the Ag target, i.e., the region where the voids are generated. The generation of voids is caused by the tensile stresses (negative pressure in a) generated in the subsurface region of the target in the lower fluence simulation (a,b) and by the internal release of vapor in the superheated molten region of the target (phase explosion) in the higher fluence simulation (c,d). The snapshots from the lower and higher fluence simulations are shown in Figures 3 and 8, respectively; the corresponding density contour plots are shown in Figures 4b and 9b. The arrows show the connection between the curves and the corresponding *y*-axes.

volume of voids is plotted along with the pressure averaged over the subsurface region where the voids are generated. The sharp increase of the number of subsurface voids coincides with the time when the dynamic relaxation of the compressive stresses produced by the laser energy deposition puts the subsurface region into tension (Figure 6a). The number of voids generated in the expanding liquid region quickly drops as the voids coalesce and coarsen, while the total volume of voids continues to increase during the first nanosecond after the laser pulse. The maximum expansion in this simulation is more than two times larger than the one observed in the regime of subsurface void generation in vacuum,[80] and the analysis of the kinetics of the solidification process provided above indicates that much larger subsurface voids can be generated in the presence of liquid environment. Note that under experimental conditions the extent of the surface swelling can be substantially larger than in the simulations performed for a small region within the laser spot. The continuity of the top liquid layer extending beyond the lateral size of the computational cell used in the simulations can further stabilize the liquid layer and extend the range of fluences that correspond to the surface swelling regime.[79,80,125]

In general, the computational prediction of the strong effect of the liquid environment on the generation of frozen surface structures is consistent with experimental observations of distinct surface morphologies generated in laser processing in liquids.[1−11] The detailed analysis of the subsurface structures, however, has not been reported for surfaces processed in liquids so far, and the prediction of the enhanced generation of larger subsurface voids and surface foaming still awaits experimental confirmation.

3.2. Generation of a Hot Metal Layer in Phase Explosion under Liquid Confinement. The second set of the simulations, illustrated in Figures 7−10, is performed at a

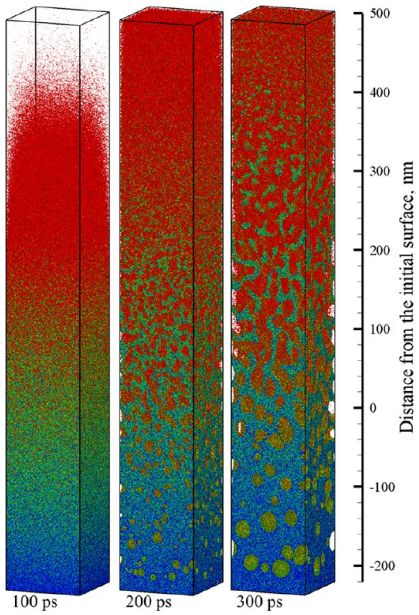

Figure 7. Snapshots of atomic configurations predicted in a simulation of a bulk Ag target irradiated *in vacuum* by a 100 fs laser pulse at an absorbed fluence of 400 mJ/cm^2. The irradiation conditions correspond to the regime of phase explosion. Only a part of the computational system from −220 to 500 nm with respect to the initial surface of the target is shown in the snapshots. The atoms are colored according to their potential energies, from blue for molten Ag to red for vapor-phase Ag atoms.

higher absorbed laser fluence of 400 mJ/cm^2, which is about twice the threshold fluence for the transition from the spallation to phase explosion regimes of laser ablation in vacuum.[75] The visual picture of the phase explosion in vacuum is shown in Figure 7. In contrast to the spallation regime, where the top part of the irradiated target remains in the liquid phase and is ejected as a thin liquid layer (Figure 2), the material ejection is driven in this case by the rapid release of vapor in the strongly superheated surface region. The very top layer of the target turns into a mixture of vapor and small atomic clusters freely expanding away from the target, while the internal release of vapor in the lower part of the target leads to the development of a fine cellular structure that rapidly decomposes into a mixture of small liquid droplets and vapor upon the expansion of the ablation plume. In the even deeper part of the plume, below the cellular structure, the propagation of tensile stresses leads to cavitation in the superheated liquid and formation of large voids, which are almost free of vapor. The expansion of

DOI: 10.1021/acs.jpcc.7b02301
J. Phys. Chem. C 2017, 121, 16549−16567

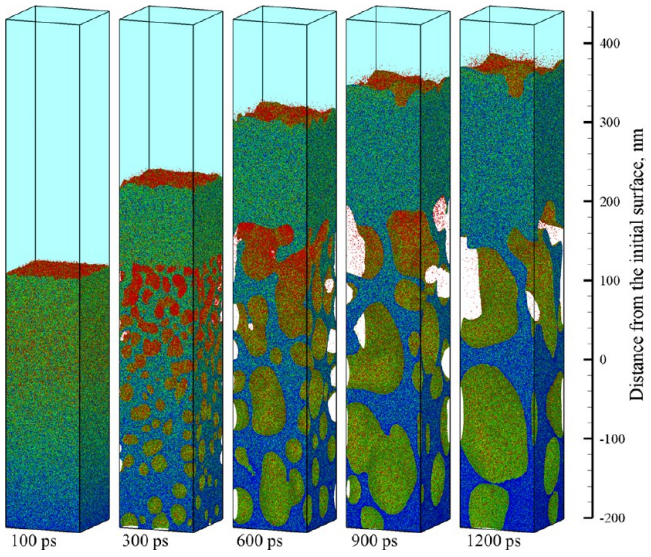

Figure 8. Snapshots of atomic configurations predicted in a simulation of a bulk Ag target irradiated *in water* by a 100 fs laser pulse at an absorbed fluence of 400 mJ/cm^2. The irradiation conditions correspond to the regime of phase explosion confined by the water environment. Only a part of the computational system from −200 to 440 nm with respect to the initial surface of the target is shown in the snapshots. The atoms are colored according to their potential energies, from blue for molten Ag to red for vapor-phase Ag atoms. The molecules representing water environment are blanked, and the presence of water is illustrated schematically by a light blue region above the Ag target.

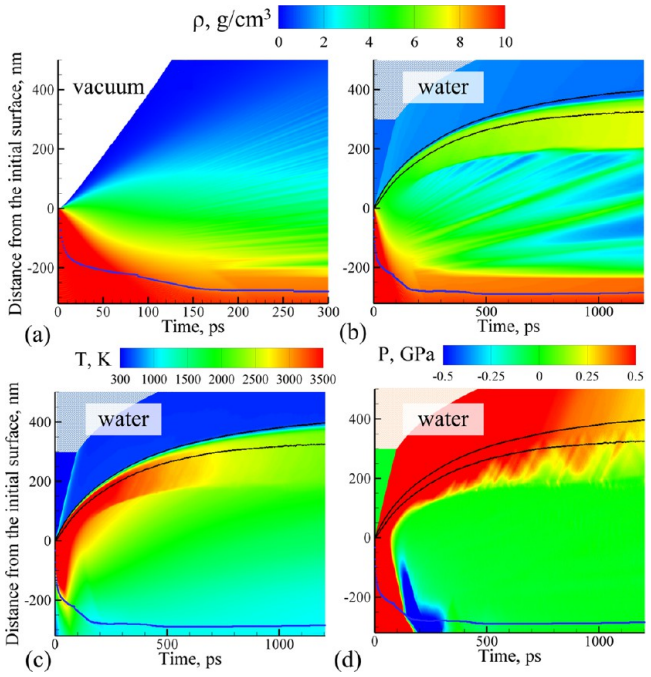

Figure 9. Density (a,b), temperature (c), and pressure (d) contour plots predicted in simulations of a bulk Ag target irradiated by a 100 fs laser pulse at an absorbed fluence of 400 mJ/cm^2 *in vacuum* (a) and *in water* (b−d). The blue line shows the location of the melting and solidification fronts. In (b−d), the two black lines outline the water−Ag mixing region defined as a region where both water molecules and Ag atoms are present. The blue (b,c) and red (d) dot background represents the presence of water beyond the pressure-transmitting boundary applied at the top of the water layer explicitly simulated with coarse-grained MD. Corresponding snapshots from the simulations are shown in Figure 7 for (a) and Figure 8 for (b−d).

this region leads to the growth and coalescence of the voids and the formation of a foamy structure of interconnected liquid regions extending in the direction of the plume expansion. The clusters and droplets generated in the phase explosion of the top part of the target and the ones emerging from photomechanical cavitation and disintegration of the deeper region have different velocities and contribute to different parts of the ablation plume, thus leading to the segregation of the clusters of different sizes in the expanding plume.[79,126]

The presence of a liquid environment drastically alters the dynamics of the formation and expansion of the ablation plume generated in the phase explosion irradiation regime, as can be seen from the simulation snapshots and the density contour plot shown in Figures 8 and 9b, respectively. The superheated molten metal that, in vacuum, undergoes an explosive decomposition into small droplets and vapor is now confined by water and is collected into a dense hot layer that pushes the water away from the target. The temperature and pressure profiles, shown in Figures 9c and 9d, indicate that the dense layer is initially brought into the supercritical state. The layer grows as the foamy subsurface region of the Ag target expands (Figure 8), and more melted and vapor phase Ag joins the layer. The colder molten Ag joining the top layer from the bottom is largely responsible for the rapid decrease of the average temperature of the layer that can be seen from Figure 9c.

Note that despite the visual similarity of the subsurface void evolution in Figures 3 and 8 the main driving forces behind the void generation in the two simulations are different, as can be clearly seen from Figures 6a and 6c. In the spallation regime, at the absorbed fluence of 150 mJ/cm^2, the sharp increase of the number of subsurface voids coincides with the time when the tensile stress, depicted by a blue line in Figure 6a, is generated in the corresponding region of the target. At the higher fluence of 400 mJ/cm^2, the superheated top layer confined by the water environment remains at positive pressure during the time when the sharp increase in the number of voids is observed (Figure 6c). This suggests that, similarly to the simulation in vacuum discussed above and illustrated by Figures 7 and 9a, the phase decomposition in the top part of the Ag target is mainly driven by the release of vapor and can be described as an explosive homogeneous boiling.[98−100] In contrast to the free expansion of the ablation plume in vacuum, however, the ejected material now accumulates into a hot layer at the interface with the water environment and exerts an outward force pushing the water away from the target, as shown in Figures 8 and 9b−d.

The water in contact with the hot metal layer formed by the ablation plume accumulation is rapidly heated to the supercritical state and provides an environment suitable for quenching and condensation of metal atoms emitted from the metal layer into the water. Note that while the temperature shown in the temperature contour plot for the water−Ag mixing region outlined by two black lines (Figures 9c) is the result of averaging over water and Ag present in this region, the two components of the mixture are far from thermal equilibrium with each other. For example, the average temperatures of Ag and water present in the mixing region at a time of 600 ps are 2665 and 1120 K, respectively. This lack of thermal equilibrium, combined with the relatively high pressure maintained in the mixing region by the dynamic metal−water

DOI: 10.1021/acs.jpcc.7b02301
J. Phys. Chem. C 2017, 121, 16549−16567

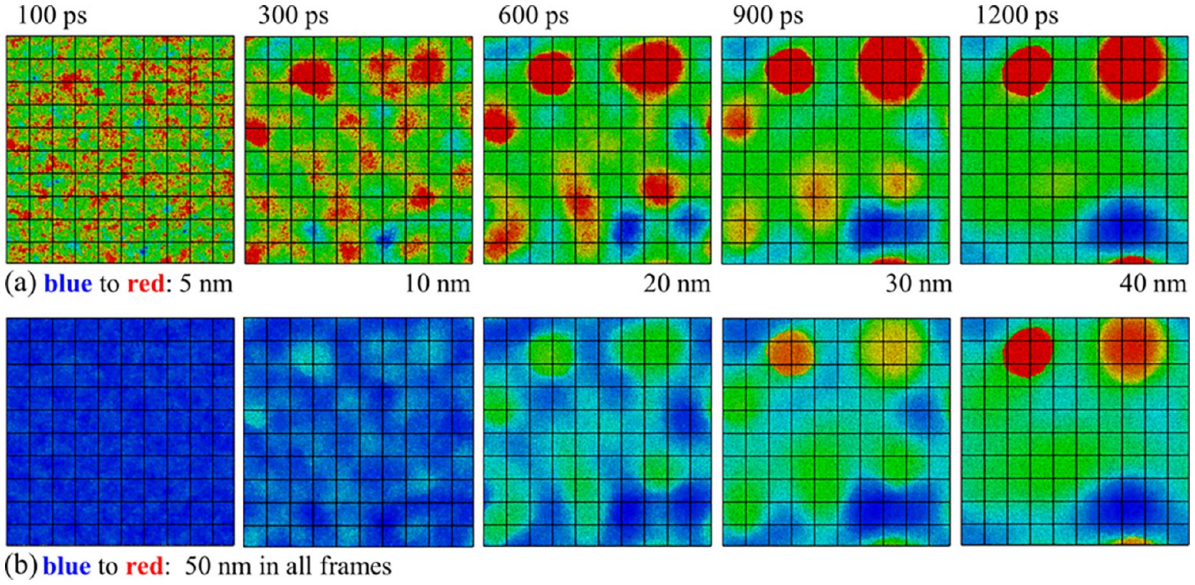

Figure 10. Topographic images of the interface between the hot metal layer and water shown for the simulation illustrated by snapshots in Figure 8. The color shows the relative height of the topographical features, with different scales used for different times in (a) to highlight the evolving interfacial roughness. The same scale of 50 nm between red and blue regions is used in all images shown in (b).

interaction (Figure 9d), keeps the thermodynamic conditions in the mixing region far from the ones required for the onset of thermal decomposition of water, as evaluated in calculation with the software package FactSage.[127]

The large temperature difference between the water and metal in the mixing region, on the other hand, facilitates the rapid condensation, cooling, and freezing of the metal nanoparticles. As has been shown in earlier simulations of thin-film ablation,[74] the condensation of metal vapor in the mixing region leads to the formation and freezing of small (mostly ≤10 nm) nanoparticles on the time scale of several nanoseconds. The beginning of this process can already be seen in the last snapshots shown in Figure 8. At a later time, beyond the time scale of the simulation, the water−silver mixing region, outlined by two black lines in Figure 9b−d, is expected to grow and to evolve into a low-density vapor region (cavitation bubble) expanding under the action of water vapor pressure.

Although by the end of the simulation, 1.2 ns, the average temperature of the hot metal layer is below the limit of stability with respect to the phase explosion, it is more than double the melting point of Ag and is only 36% below the threshold for the phase explosion at zero pressure.[75] The layer may slowly cool due to the interaction with water, evaporation, and, if the bridges connecting the layer to the bulk of the target remain, through the heat conduction to the target. It is quite likely, however, that the hot metal layer would rupture and disintegrate into large liquid droplets due to the inherent instability of thin liquid films,[79,128,129] the dynamic interaction of the liquid metal layer with the expanding and collapsing vapor bubble, and the emergence of Rayleigh−Taylor instability at the metal−water interface. The latter mechanism is responsible for the rapid development of complex morphology of the metal−water interface that can be seen from snapshots shown in Figure 8 and plays an important role in the layer decomposition. Therefore, the origin of the Rayleigh−Taylor instability is discussed in more detail in the next section.

The onset of the nucleation and growth of small nanoparticles in the metal−water mixing region and the likely breakup of the hot metal layer into large droplets represent two distinct mechanisms of the nanoparticle formation that are likely to yield nanoparticles of two different size ranges. This computational prediction is consistent with the observation of bimodal nanoparticle size distributions in femtosecond PLAL experiments,[15,16] where small nanoparticles with sizes less than or around ten nanometers are found to coexist with larger (tens to hundreds of nanometers) ones. The high computational cost of large-scale atomistic simulations, the limited lateral size of the computational cell, and the relatively long time scales associated with both of the aforementioned mechanisms prevent us from directly observing the nanoparticle formation in the simulation discussed in this section. Faster generation of the nanoparticles through the same two mechanisms, however, has been observed in simulations of PLAL of thin films,[74] ablation of bulk targets at a higher fluence (to be reported elsewhere), and second pulse ablation of targets modified by the first pulse (discussed in Section 3.4).

3.3. Rayleigh−Taylor Instability at the Metal−Water Interface. One of the key processes that may lead (or contribute) to the disintegration of the molten metal layer generated due to the confinement of the ablation plume by the water environment is the development of Rayleigh−Taylor instability at the metal−water interface. The rapid deceleration of the denser metal layer by the pressure exerted from the lighter supercritical water creates conditions corresponding to the classical picture of the Rayleigh−Taylor instability, where the acceleration of the interface and density gradient have the same directions. The fastest growing wavelength λ_m and the characteristic time τ of the exponential growth of small perturbations in the Rayleigh−Taylor instability can be estimated based on the linear stability analysis applied to inviscid fluids[130,131]

$$\lambda_m = 2\pi\left[\frac{3\sigma}{(\rho_{ml} - \rho_w)G}\right]^{1/2} \quad (1)$$

DOI: 10.1021/acs.jpcc.7b02301
J. Phys. Chem. C 2017, 121, 16549−16567

$$\tau = \left[\frac{2}{3}kAG\right]^{-1/2} = \left[\frac{2}{3^{3/2}}\frac{(\rho_{ml} - \rho_w)^{3/2}G^{3/2}}{(\rho_{ml} + \rho_w)\sigma^{1/2}}\right]^{-1/2} \quad (2)$$

where $k = 2\pi/\lambda_m$ is the wave vector; $A = (\rho_{ml} - \rho_w)/(\rho_{ml} + \rho_w)$ is the Atwood number; ρ_{ml} and ρ_w are the densities of the heavier and lighter fluids (metal layer and supercritical water); σ is the interfacial tension; and G is the effective acceleration of the interface in the direction pointing into the heavier fluid.

In the simulation of PLAL discussed in the previous section, the deceleration of the metal layer by the water overlayer can be seen from the density contour plot shown in Figure 9b. The deceleration is not constant but rapidly changes from the maximum value of $\sim 7 \times 10^{12}$ m/s^2 recorded at 40 ps down to 1.6×10^{12} m/s^2 at 300 ps and then to 3.0×10^{11} m/s^2 by the end of the first nanosecond after the laser pulse. The densities of the compressed supercritical water, ρ_w, and the hot metal layer, ρ_{ml}, are also changing during the simulation. These changes, however, are relatively small, and average values of $\rho_w = 1.2$ g/cm^3 and $\rho_{ml} = 7$ g/cm^3 are used in the estimations of λ_m and τ. The temperature dependence of the interfacial tension is also neglected, and the value of $\sigma = 0.09$ J/m^2 evaluated for the model Ag–water system at 1800 K using the test-area simulation method[132] is adopted in the estimations. Using these parameters in eqs 1 and 2, we obtain $\lambda_m = 33.9$ nm and $\tau = 85$ ps for the layer deceleration of 1.6×10^{12} m/s^2 at 300 ps and $\lambda_m = 78.3$ nm and $\tau = 297$ ps for the lower deceleration of 3.0×10^{11} m/s^2 at 1 ns.

To compare the above estimations with the results of the simulation discussed in the previous section, the evolution of morphology of the interface is shown in Figure 10 for the same moments of time for which the snapshots are shown in Figure 8. In a semiquantitative agreement with the theoretical estimations, the initial fine roughness of the interface with characteristic spatial dimension on the order of several nanometers appears as early as 100 ps and gradually evolves into a coarser interface morphology with characteristic length scale of several tens of nanometers. The observation of the emergence of the nanoscale interface morphology on the time scale of hundreds of picoseconds through the Rayleigh–Taylor instability is in agreement with the results of earlier MD simulations[133,134] and is a clear indication that nanoscale hydrodynamic instability is likely to play an important role in the nanoparticle generation in PLAL. Indeed, in recent simulations of thin metal film ablation in liquids,[74] the Rayleigh–Taylor instability has been shown to result in disintegration of a molten metal layer and generation of large droplets. Another demonstration of the key role of the Rayleigh–Taylor instability in the generation of large metal nanoparticles in PLAL is provided in the next section.

Note that the initial development of the interface roughness due to the Rayleigh–Taylor instability and the subsequent nonlinear evolution of the interface morphology are sensitive to the viscosity, density ratio, and the variation of the acceleration of the two fluid layers. This sensitivity suggests that the characteristics of the nanoparticles generated through the Rayleigh–Taylor instability at the plume–liquid environment interface can be, to a certain extent, controlled by choosing the ablation target, liquid environment, and irradiation parameters.

3.4. Generation of Nanoparticles by the Second Pulse Irradiation. The results of the simulations discussed in Section 3.1 predict that the final structure of a surface region of a target irradiated in the regime of spallation confined by liquid environment, below the threshold for nanoparticle formation, is essentially a thin metal layer loosely connected to the bulk of the target by thin walls and bridges, similar to the configuration shown for a partially solidified target in the last snapshot in Figure 3. The formation of porous surface morphology is also possible at higher fluences, in the phase explosion regime discussed in section 3.2, when the hot metal layer generated at the front of the ablation plume (e.g., Figure 8) does not disintegrate into nanoparticles but cools due to the interaction with liquid environment and heat conduction to the bulk of the target. The irradiation of such targets by a subsequent laser pulse would result in spatial localization of the deposited laser energy within the top surface layer of the target and may lead to a substantial reduction of the threshold fluence for the generation of nanoparticles. Thus, the presence of large subsurface voids can facilitate generation of nanoparticles in the multipulse irradiation regime at fluences that do not produce nanoparticles upon irradiation with a single pulse, leading to the so-called incubation effect. The incubation effect has been extensively studied for vacuum conditions,[135−139] and as shown in a recent computational study,[80] the generation of subsurface voids may be one of the mechanisms responsible for the incubation. The response of a target with subsurface voids to the irradiation in a liquid environment, when the material expansion is suppressed by the presence of the liquid overlayer, however, has not been investigated so far.

To explore the effect of the presence of subsurface voids on the microscopic mechanisms of pulsed laser ablation in liquids, a sample mimicking a frozen film connected to the bulk of the target by thin bridges is constructed based on the predictions of the simulations discussed in Sections 3.1 and 3.2. The top part of the sample is shown in the first frame of Figure 11. The sample is irradiated by a laser pulse with duration of $\tau_L = 100$ fs and absorbed fluence of $F_{abs} = 300$ mJ/cm^2, which is below the threshold for the generation of large nanoparticles in a single pulse laser irradiation in water.

The results of the simulation are illustrated by a series of snapshots shown in Figure 11, which reveals rich dynamics of the superheated material undergoing an explosive decomposition into liquid and vapor. The deposition of laser energy is largely localized within the top thin layer that covers the underlying void. The superheated layer undergoes phase explosion and expands in both directions, as schematically shown by the two arrows on the density contour plot in Figure 12a. Similar to the simulation discussed in section 3.2, the upward expansion of the top part of the film is decelerated by the water environment, and the products of the phase explosion (Ag vapor and small clusters) are accumulated at the plume–water interface forming a hot metal layer. The downward expansion of the bottom part of the film results in a rapid collapse of the void within the first ~40 ps after the laser pulse and is followed by formation of two vortexes on both sides of the thin wall that connected the initial top layer with the bulk of the target, as depicted in Figure 13. The heating and lateral compression of the thin wall by the colliding vortexes rapidly melt and accelerate the wall material in the vertical direction, leading to the disintegration of the wall by ~1 ns (Figure 11). The rebound of the hot plume from the wall leads to the formation of low-density vapor regions near the wall by 200 ps (Figures 11 and 13) and accumulation of the material in the central part of the original void (snapshot for 500 ps in Figure 11). The net result of the complex material flow dynamics illustrated in Figure 13 is the overall upward acceleration

DOI: 10.1021/acs.jpcc.7b02301
J. Phys. Chem. C 2017, 121, 16549−16567

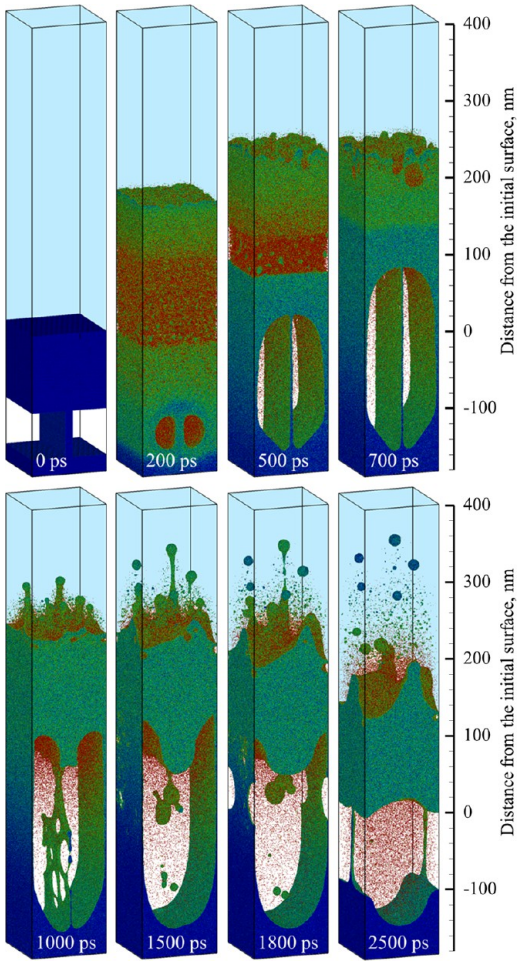

Figure 11. Snapshots of atomic configurations predicted in a simulation of a bulk Ag target with a subsurface void irradiated *in water* by a 100 fs laser pulse at an absorbed fluence of 300 mJ/cm^2. The irradiation conditions correspond to the regime of phase explosion confined by the water environment. Only a part of the computational system from −180 to 400 nm with respect to the initial surface of the target is shown in the snapshots. The atoms are colored according to their potential energies, from blue for solid Ag to green for molten Ag and red for vapor-phase Ag atoms. The molecules representing water environment are blanked, and the presence of water is illustrated schematically by a light blue region above the Ag target. Animated sequence of snapshots from this simulation with a time resolution of 100 ps is provided as Supporting Information for this article.

(rebound) of the lower part of the plume from the bulk of the target, as shown by the lower arrow in Figure 12a.

The rebounded material moves up and eventually makes an impact on the floating molten layer formed by accumulation of the upper part of the phase explosion plume at the interface with the water environment. The impact occurs at ~800 ps and results in the formation of several nanojets rapidly extending into the water environment. These nanojets elongate toward the colder water region and rupture to produce large droplets/nanoparticles with diameters on the order of tens of nanometers. A total of eight large nanoparticles are formed through the breakup of multiple liquid nanojets, with some of the nanojets producing more than one nanoparticle, as can be seen from the snapshots in Figure 14 that are focused on the metal−water interface (region between two dashed red lines in Figure 12) and the time span when the nanojets are generated.

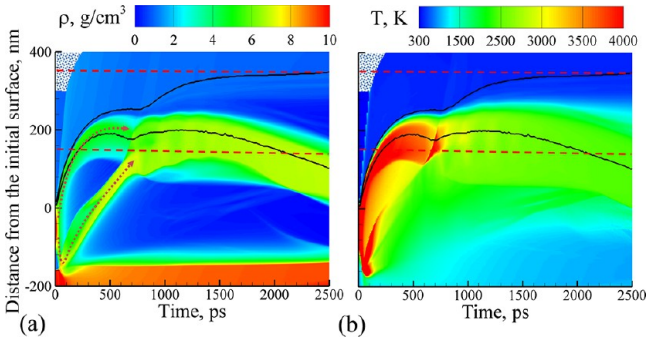

Figure 12. Density (a) and temperature (b) contour plots predicted in a simulation of a bulk Ag target with a subsurface void irradiated *in water* by a 100 fs laser pulse at an absorbed fluence of 300 mJ/cm^2. The two black lines outline the water−Ag mixing region defined as a region where both water molecules and Ag atoms are present. The blue dot background in the upper left corners of the plots represents the presence of water beyond the pressure-transmitting boundary applied at the top of the water layer explicitly simulated with coarse-grained MD. The two dashed orange arrows in (a) show schematically the colliding trajectories of the hot molten layer generated at the interface with water environment and a colder molten layer approaching it from the bottom. The two horizontal dashed red lines outline the region for which snapshots of atomic configurations are shown in Figure 14.

The diameters and the corresponding numbers of atoms in the eight large nanoparticles at a time of 2.5 ns are as follows: 15.8 nm (119 909 atoms), 14.3 nm (89 496 atoms), 13.1 nm (67 936 atoms), 12.3 nm (57 349 atoms), 11.1 nm (41 683 atoms), 11.0 nm (40 799 atoms), 10.0 nm (30 761 atoms), and 9.8 nm (29 073 atoms).

The lower row of snapshots in Figure 14 shows the origin of atoms that end up in each of the eight nanoparticles. It can be seen that before the impact from the rebounded material all the atoms that contribute to the large nanoparticles are already present inside the liquid layer and are mostly located within the trough regions of the layer, suggesting that the roughness of the interface plays an essential role in the formation of the nanoparticles. Moreover, consideration of an overlap of the shapes of the interface before and after the rebounded materials impact (700 and 1100 ps, respectively), shown in Figure 15, clearly demonstrates that the liquid nanojets are ejected out from the trough areas of the interface.

As discussed in Section 3.3, the initial roughness of the water−metal interface is produced through the Rayleigh−Taylor instability of the interface undergoing strong deceleration directed from the lighter supercritical water toward the heavier hot metal layer. By applying analysis described in Section 3.3 and using the values of deceleration and densities measured at 500 ps after the laser pulse in eqs 1 and 2, the wavelength and time scale of the Rayleigh−Taylor instability are estimated to be λ_m = 64.2 nm and τ = 200 ps. These values are in a reasonable semiquantitative agreement with the interface roughness that can be seen in the snapshots shown for 200 and 500 ps in Figure 11.

With the formation of the roughened water−metal interface serving as the first step in the generation of large nanoparticles, the second step is the emission of nanojets induced by the backside impact of the rebounded material. The formation of the nanojets can be described in terms of Richtmyer−Meshkov instability that occurs when a shock wave impinges a roughened interface between materials of different density.[140] The shock-

DOI: 10.1021/acs.jpcc.7b02301
J. Phys. Chem. C 2017, 121, 16549−16567

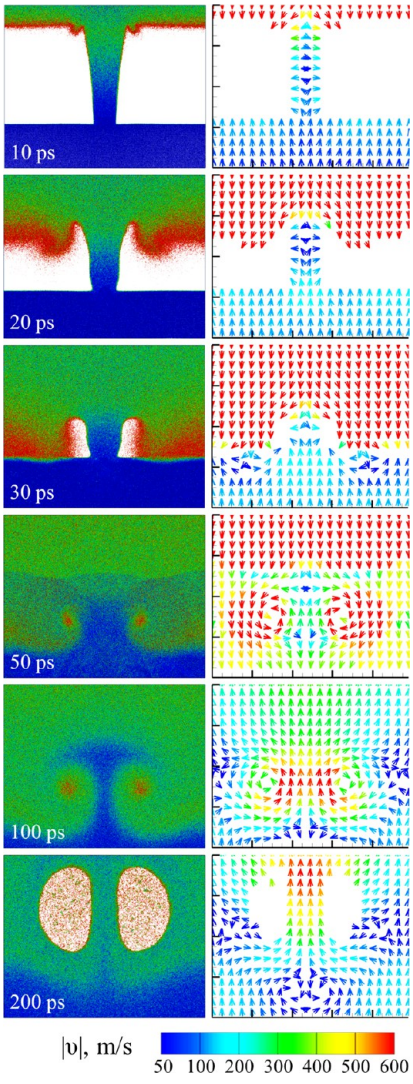

Figure 13. Snapshots of atomic configurations (left column) and fields of the material flow velocities (right column) highlighting the void collapse and vortex formation in a simulation of a bulk Ag target with a subsurface void irradiated *in water* by a 100 fs laser pulse at an absorbed fluence of 300 mJ/cm^2. Only a part of the computational system from −100 to −180 nm with respect to the initial surface of the target is shown in the snapshots. The atoms in the snapshots are colored according to their potential energies, from blue for molten Ag to red for vapor-phase Ag atoms. The magnitude of the flow velocities is shown by color with scale provided at the bottom of the figure.

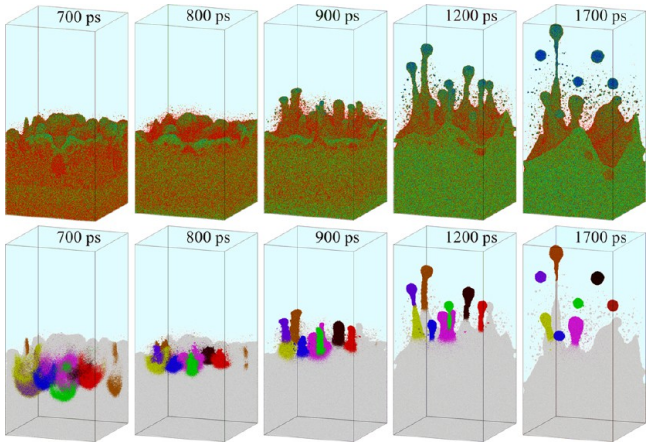

Figure 14. Snapshots of the evolution of the hot metal layer−water interface predicted in a simulation of a bulk Ag target with a subsurface void irradiated *in water* by a 100 fs laser pulse at an absorbed fluence of 300 mJ/cm^2. The snapshots are shown for a part of the computational system from 150 to 350 nm with respect to the initial surface of the target (i.e., the region outlined by two dashed red lines in Figure 12) and for a time interval when several large (10s of nm in diameter) nanoparticles are ejected from the hot metal layer into the water environment. In the upper row, the atoms in the snapshots are colored according to their potential energies, from green for molten Ag to red for individual Ag atoms. In the lower row, the atoms are colored by nanoparticle ID defined by the contribution of atoms to one of the eight large nanoparticles ejected into the water environment via the Rayleigh−Taylor instability (each color except gray corresponds to atoms that end up in one of the eight nanoparticles). The molecules representing water environment are blanked in all snapshots.

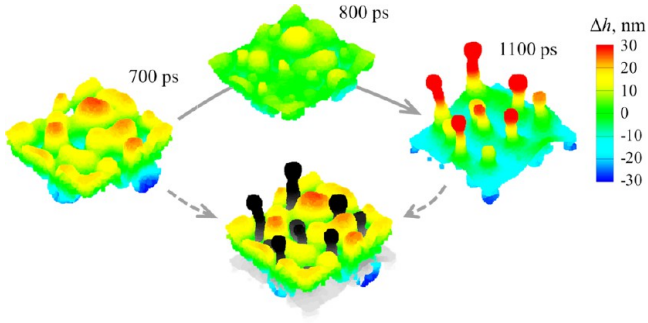

Figure 15. Result of the surface reconstruction performed for the hot metal layer−water interface that can be seen in the snapshots in Figures 11 and 14. The overlapped view of two surfaces reconstructed for 700 and 1100 ps is shown in the lower part of the figure, with the surface for 1100 ps colored using gray scale.

driven inversion of the initial surface perturbations and formation of jets extending into lower-density medium have been analyzed theoretically[141,142] and investigated in atomistic and hydrodynamic simulations.[143−145] The location of the nanojets and the dynamic material redistribution from the troughs of the interface to the nanojets are consistent with the results of the prior studies. Finally, the extension of the nanojets results in the separation of droplets in a process that can be attributed to the capillary (Plateau−Rayleigh) instabilities driven by the surface tension,[146,147] with water environment certainly playing an important role in defining the dynamics of the nanojet extension and separation of the droplets.

The new mechanism of the nanoparticle generation revealed in the simulation and discussed above demonstrates that the nucleation and growth from the vapor phase, which is also observed in this simulation (see discussion below and Figure 16), is not the only possible channel of nanoparticle generation at the early stage of PLAL. While the cascade of the hydrodynamic instabilities responsible for the ejection of the eight nanoparticles into the water environment in the present simulation may look somewhat exotic, the results of the simulations performed for other systems suggest that it is not unique to the target with subsurface voids. In particular, a similar phenomenon has also been observed in a simulation of high fluence short pulse laser ablation of a void-free bulk Ag target in water (to be reported elsewhere), where a spalled layer coming from the deeper part of the target and joining the hot metal layer formed at the interface with the water environment provides the external impact that leads to the jetting and

DOI: 10.1021/acs.jpcc.7b02301
J. Phys. Chem. C 2017, 121, 16549−16567

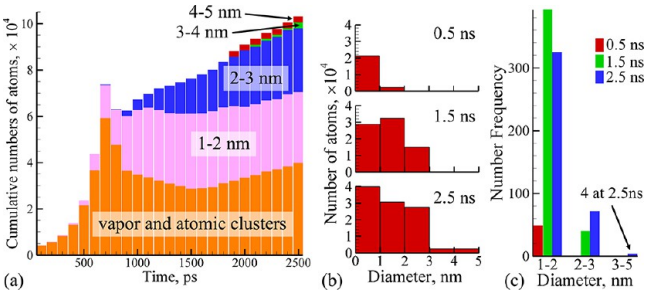

Figure 16. Results of the cluster analysis applied to the Ag content of the Ag–water mixing region generated in a simulation of a bulk Ag target with a subsurface void irradiated *in water* by a 100 fs laser pulse at an absorbed fluence of 300 mJ/cm^2. The cumulative number of individual Ag atoms and small clusters with diameters less than 1 nm (orange) and the cumulative numbers of atoms that belong to nanoparticles of different sizes (above 1 nm) are shown in (a). The number of atoms in atomic clusters and nanoparticles of different sizes are shown as histograms for 0.5, 1.5, and 2.5 ns in (b). The number of nanoparticles of different sizes is also shown for the same moments of time in (c).

generation of large nanoparticles. Moreover, the roughening of the metal–water interface through the Rayleigh–Taylor instability combined with the general limited stability of thin liquid films[79,128,129] may result in direct production of large nanoparticles, as have been observed in a recent simulation of laser ablation of a thin Ag film in water.[74]

As mentioned above, another general mechanism of nanoparticle generation observed in the simulation is the nucleation and growth from the Ag vapor in the low-density mixing region generated due to the interaction of water with the hot metal layer and evaporation of Ag atoms from the metal layer. The expanding metal–water mixing region is outlined by two black lines in Figure 12. As seen from Figure 12b, the average temperature in the mixing regions, while staying above the critical temperature of water, is close to and, in the upper part, even below the melting temperature of Ag. Hence, the vapor Ag atoms rapidly condense, forming small nanoparticles (up to several nanometers in diameter) on a very short time scale of just several nanoseconds after the laser irradiation. Moreover, some of the nanoparticles located in the upper part of the mixing region solidify on the time scale of the simulation, 2.5 ns. The kinetics of nanoparticle formation through the nucleation and growth in the mixing region is illustrated in Figure 16 and discussed below.

The analysis of the evolution of sizes of the metal clusters and nanoparticles in the mixing region is performed with a cluster identification algorithm applied to atomic configurations generated in the simulation between 100 and 2500 ps, with a 100 ps interval. The eight large nanoparticles separated from the liquid nanojets are not considered in this analysis. The evolution of the cumulative number of Ag atoms present above the liquid layer as individual atoms (vapor) and small atomic clusters with diameters below 1 nm (less than 30 atoms) as well as the larger clusters that we denote as nanoparticles is shown in Figure 16a. While the total number of Ag atoms in the mixing region steadily increases due to the continuous evaporation from the hot molten metal layer, the number of atoms in the Ag vapor and atomic clusters stays at approximately the same level starting from 1 ns, and the increase in the total number of Ag atoms in the mixing region is largely sustained by the growing populations of nanometer-scale nanoparticles. Note that the number of vapor-phase atoms and atomic clusters shows an apparent drop at around 800 ps, when the mixing region undergoes a transient compression due to the impact of the rebounded material from the backside of the hot metal layer (Figure 12). The compression makes some of the ejected metal atoms rejoin the metal layer, as suggested by the small temporal drop of the total number of Ag atoms in the mixing region, but also facilitates the condensation of vapor and coalescence of clusters into the nanoparticles. Overall, the nanoparticle size distribution broadens and shifts to the larger sizes as time progresses, as can be seen from the nanoparticle size distributions shown in Figure 16b,c. While the growth of the nanoparticles is still ongoing at the end of the simulation, the size of the nanoparticles generated through the nucleation and growth in the metal–water mixing region can be expected to mostly remain below 10 nm. This size is consistent with experimental observation of the generation of small (<10 nm) nanoparticles in femtosecond laser ablation of gold[15] and silver[148] targets in pure water. An inspection of the enlarged view of the metal–water mixing region shown in Figure 17a

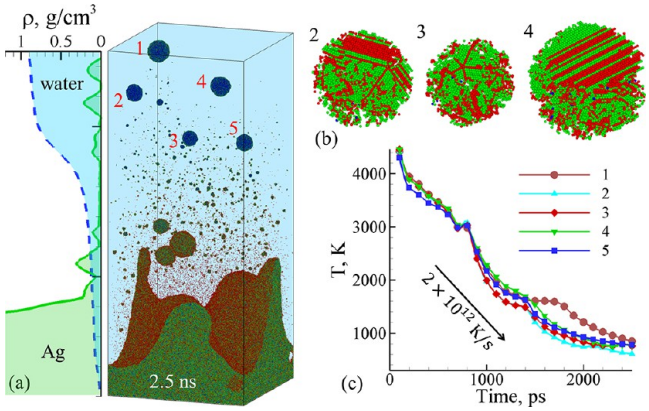

Figure 17. (a) Snapshot of a part of the final atomic configuration (from 120 to 350 nm with respect to the initial surface of the target) and the corresponding plots of water and silver densities (blue dashed and green solid curves, respectively) in the simulation illustrated by Figures 11–16. The atoms in the snapshot are colored by their potential energies, from blue for solid Ag to green for molten Ag and to red for vapor-phase Ag atoms. The molecules representing water environment are blanked in the snapshot. Five out of eight large (10s of nanometers) nanoparticles generated via Rayleigh–Taylor and Richtmyer–Meshkov instabilities had already crystallized by the end of the simulation and are indexed in the snapshot. The structure of three of these five nanoparticles is shown in (b), where the atoms are colored according to their local structural environment, so that the fcc, hcp, and bcc atoms are green, red, and blue, respectively, while the atoms that belong to the crystal defects and surfaces are blanked. The time dependence of the average temperature of atoms that end up in the five nanoparticles indexed in (a) is shown in (c).

indicates that the largest nanoparticles formed through the nucleation and growth are mostly found in the middle part of the mixing region, where the sufficiently low temperature of the water environment and the high Ag vapor concentration provide the optimum conditions for condensation into Ag nanoparticles.

An important characteristic of the nanoparticle generation in PLAL, common to both mechanisms revealed in the simulations, is the rapid quenching of the nanoparticles inside the water–metal mixing region. The interaction between the hot metal vapor and water not only brings the water to the

DOI: 10.1021/acs.jpcc.7b02301
J. Phys. Chem. C 2017, 121, 16549–16567

supercritical state but also rapidly cools the metal vapor and nanoparticles down to the temperature that can be sufficiently low to cause solidification of large nanoparticles. As one can see from Figure 17a, the small nanoparticles in the upper part of the mixing region are colored blue, indicating the low level of potential energy that is characteristic of the crystalline state. Indeed, similarly to the small nanoparticles generated through the nucleation and growth in the earlier simulation of PLAL of a thin Ag film,[74] the small nanoparticles in the upper part of the mixing region are found to crystallize within the first nanoseconds after the laser pulse.

The larger nanoparticles produced from the droplets separated from the nanojets also experience a very rapid quenching and solidification. Indeed, five of the nanoparticles labeled as 1 to 5 in Figure 17a are already solidified by the end of the simulation. The nanojets generated through the Richtmyer−Meshkov instability of the roughened interface are launching the droplets past the low-density part of the mixing region directly into the denser and colder water environment, as can be seen from the density plots shown in Figure 17a. The droplets then quickly cool and solidify through the interaction with water. The thermal history of the material contributing to the five nanoparticles injected into the dense water region is shown in Figure 17c, where the effective cooling rate in excess of 10^{12} K/s is observed. The high cooling rate is enabled by the suppression of the formation of an insulating vapor layer around the hot droplets by the high curvatures of the droplet−water interfaces, an effect that has been demonstrated in MD simulations of heat transfer from hot nanoparticles to a surrounding liquid.[149,150] As a result, very high heat fluxes from the hot droplets to the water environment are sustained, the metal droplets are strongly undercooled, and the crystallization of the nanoparticles is activated within just several hundreds of picoseconds. A similar time scale of crystallization has recently been reported in MD simulations of the solidification of ZnO nanoparticles in a liquid environment.[151]

The structural analysis of the frozen nanoparticles reveals polycrystalline structure with multiple stacking faults, twin boundaries, and pentagonal twinned domains, as well as platelets of metastable hcp structure, as illustrated by images of three nanoparticles shown in Figure 17b. A similar complex nanostructure has been observed in a frozen nanospike generated in a simulation of laser spallation of a Ag target[81] and attributed to the highly nonequilibrium nature of the rapid nucleation and growth of new crystallites that takes place under conditions of deep undercooling,[80,81] along with the low stacking-fault energy of Ag.[152] The polycrystalline structure has also been experimentally observed in Ag nanoparticles generated in femtosecond pulse laser ablation of a solid Ag target in water,[148] i.e., for conditions similar to the ones used in the present simulations. In general, the ultrafast quenching and solidification rates suggest that PLAL can be an effective technique to generate nanoparticles with highly nonequilibrium metastable structures and phases.

The computational prediction of the existence of two distinct mechanisms of nanoparticle formation is consistent with experimental observations of bimodal nanoparticle size distributions in femtosecond PLAL[15,16] and can be related to the results of recent time-resolved SAXS probing of the cavitation bubble dynamics,[63−66] where two groups of nanoparticles, with different characteristic sizes, have been observed to emerge at different stages of the bubble evolution. The SAXS experiments are performed with nanosecond laser pulses, where the formation of the hot molten metal layer at the interface with the liquid environment and the corresponding production of larger "secondary" nanoparticles through the breakup of the molten layer still await verification in the simulations. Nevertheless, the "primary" nanoparticles with sizes below 10 nm are likely to be generated through the same mechanism as the small nanoparticles in the simulations, i.e., the rapid nucleation and growth in the expanding mixing region. The recent experimental confirmation that both primary and secondary nanoparticles are present at the early stage of the cavitation bubble expansion[66] is providing an additional support to this association between the computational predictions and experimental observations.

4. SUMMARY

Large-scale atomistic simulations are used in this work to investigate the physical mechanisms and processes responsible for the modification of surface structure and generation of nanoparticles in short pulse laser interactions with bulk metal targets in a liquid environment. The simulations are performed with a computational model combining a coarse-grained representation of liquid (parametrized for water), a fully atomistic description of laser interactions with metal targets, and acoustic impedance matching boundary conditions designed to mimic nonreflecting propagation of laser-induced pressure waves through the boundaries of the computational domain. The model is implemented in a computationally efficient parallel code, which is used to perform a series of simulations of femtosecond pulse laser ablation and processing of bulk Ag targets. The results of the simulations performed in the irradiation regimes that correspond to photomechanical spallation and phase explosion in vacuum have revealed the strong effect of the liquid environment on the modification of surface regions of the irradiated targets and generation of nanoparticles of different sizes. The main findings of the computational study are summarized below.

1. *Generation of large subsurface voids and surface swelling*: For the irradiation conditions that correspond to the spallation regime in vacuum, the simulations performed in water predict that the interaction with water environment can prevent the complete separation of spalled molten layer from the target, resulting in the formation of much larger frozen-in subsurface voids as compared to ones observed in simulations performed close to the spallation threshold in vacuum. Moreover, the confinement by liquid environment can significantly broaden the fluence range for the formation of large subsurface voids, produce more extensive surface swelling, and result in the formation of unique surface morphologies.

2. *Phase explosion under liquid confinement—buildup of a hot metal layer at the front of the ablation plume*: The simulations performed at higher laser fluences, that correspond to the phase explosion regime in vacuum, reveal the accumulation of the ablation plume at the interface with the water environment and formation of a hot metal layer. The water in contact with the metal layer is brought to the supercritical state, expands, and absorbs metal atoms emitted from the hot metal layer. The expanding low density metal−water mixing region provides an environment suitable for rapid nucleation and growth of small metal nanoparticles and serves as a precursor for the formation of a cavitation bubble.

3. *Hydrodynamic instabilities and disintegration of the metal layer*: The hot metal layer generated due to the confinement of

DOI: 10.1021/acs.jpcc.7b02301
J. Phys. Chem. C 2017, 121, 16549−16567

the ablation plume by the liquid environment has limited stability and can readily disintegrate into large (tens of nanometers) nanoparticles. The layer disintegration is facilitated by Rayleigh−Taylor instability of the interface between the higher density metal layer decelerated by the pressure from the lighter supercritical water, which creates an extensive nanoscale surface roughness of the interface on a time scale of hundreds of picoseconds. Moreover, the backside impact of the material joining the hot molten layer at a later time can induce Richtmyer−Meshkov instability of the roughened interface and result in the formation of nanojets launching large droplets through the low-density mixing region directly into denser and colder water environment.

4. *Bimodal nanoparticle size distribution*: Rapid nucleation and growth of small nanoparticles in the metal−water mixing region and the breakup of the hot metal layer into larger droplets due to the hydrodynamic instabilities represent two distinct mechanisms of the nanoparticle formation that yield nanoparticles of two different size ranges as early as several nanoseconds after the laser irradiation. This computational prediction provides a plausible explanation for experimental observations of bimodal nanoparticle size distributions in femtosecond PLAL experiments.

5. *Rapid quenching and solidification of nanoparticles*: The thermodynamic conditions in the expanding metal−water mixing region not only facilitate rapid nucleation and growth of metal clusters and nanoparticles but also ensure highly efficient cooling and solidification of the nanoparticles that are found to crystallize within the first nanoseconds after the laser pulse. The larger nanoparticles produced through the hot molten metal layer disintegration and injected into the water environment are also rapidly cooled and solidified, with cooling rates in excess of 10^{12} K/s observed in the simulations. The ultrahigh cooling and solidification rates suggest the possibility for generation of nanoparticles featuring metastable phases and highly nonequilibrium structures.

6. *Incubation effect in multipulse laser ablation*: The generation of subsurface voids or, at higher fluences, an extended porous surface morphology can strongly modify the processes induced by subsequent laser pulses applied to the same area on the target. Spatial localization of the deposited laser energy within the top surface layer partially insulated from the bulk of the target by the subsurface voids is shown to result in a substantial reduction of the threshold fluence for the explosive material disintegration and generation of nanoparticles. The reduction of the threshold for the material ablation and nanoparticle generation can be related to the incubation effect in the multipulse laser ablation in liquids.

Overall, the first atomistic simulations of laser ablation of bulk metal targets in water have provided important insights into the complex phenomenon of laser−material interactions in liquid environment and revealed an array of mechanisms and processes that are unique for laser ablation in liquids. The emerging understanding of laser-induced processes is likely to facilitate the intelligent design of new PLAL setups capable of controlled generation of nanoparticles and surface structures characterized by unusual nonequilibrium structure and phase composition.

■ ASSOCIATED CONTENT

Supporting Information

The Supporting Information is available free of charge on the ACS Publications website at DOI: 10.1021/acs.jpcc.7b02301.

Animated sequence of snapshots from a simulation illustrated in Figure 11. The snapshots in the animation are shown with a time resolution of 100 ps. (ZIP)

■ AUTHOR INFORMATION

Corresponding Author

*E-mail: lz2n@virginia.edu.

ORCID

Leonid V. Zhigilei: 0000-0002-1549-7086

Notes

The authors declare no competing financial interest.

■ ACKNOWLEDGMENTS

Financial support for this work was provided by the National Science Foundation (NSF) through Grants CMMI-1301298 and DMR-1610936. Computational support was provided by the Oak Ridge Leadership Computing Facility (INCITE project MAT130) and NSF through the Extreme Science and Engineering Discovery Environment (project TG-DMR110090). L.V.Z. acknowledges support from the Austrian Science Fund (FWF) through the Lise Meitner Programme (project M 1984). C.-Y.S. acknowledges visiting researcher support from the Center for Nanointegration Duisburg-Essen (CENIDE), University of Duisburg-Essen, Germany. The authors also acknowledge assistance with advanced visualization provided by Benjamin Hernandez Arreguin and Michael A. Matheson of Oak Ridge National Laboratory.

■ REFERENCES

(1) Zavedeev, E. V.; Petrovskaya, A. V.; Simakin, A. V.; Shafeev, G. A. Formation of Nanostructures Upon Laser Ablation of Silver in Liquids. *Quantum Electron.* **2006**, *36*, 978−980.

(2) Truong, S. L.; Levi, G.; Bozon-Verduraz, F.; Petrovskaya, A. V.; Simakin, A. V.; Shafeev, G. A. Generation of Ag Nanospikes Via Laser Ablation in Liquid Environment and Their Activity in SERS of Organic Molecules. *Appl. Phys. A: Mater. Sci. Process.* **2007**, *89*, 373−376.

(3) Stratakis, E.; Zorba, V.; Barberoglou, M.; Fotakis, C.; Shafeev, G. A. Laser Writing of Nanostructures on Bulk Al Via Its Ablation in Liquids. *Nanotechnology* **2009**, *20*, 105303.

(4) Barmina, E. V.; Stratakis, E.; Fotakis, K.; Shafeev, G. Generation of Nanostructures on Metals by Laser Ablation in Liquids: New Results. *Quantum Electron.* **2010**, *40*, 1012−1020.

(5) Podagatlapalli, G. K.; Hamad, S.; Sreedhar, S.; Tewari, S. P.; Rao, S. V. Fabrication and Characterization of Aluminum Nanostructures and Nanoparticles Obtained Using Femtosecond Ablation Technique. *Chem. Phys. Lett.* **2012**, *530*, 93−97.

(6) Bashir, S.; Rafique, M. S.; Nathala, C. S.; Husinsky, W. Surface and Structural Modifications of Titanium Induced by Various Pulse Energies of a Femtosecond Laser in Liquid and Dry Environment. *Appl. Phys. A: Mater. Sci. Process.* **2014**, *114*, 243−251.

(7) Bashir, S.; Rafique, M. S.; Nathala, C. S.; Husinsky, W. The Formation of Nanodimensional Structures on the Surface of Tin Exposed to Femtosecond Laser Pulses in the Ambient Environment of Ethanol. *Appl. Surf. Sci.* **2014**, *290*, 53−58.

(8) Barmina, E. V.; Shafeev, G. A.; Kuzmin, P. G.; Serkov, A. A.; Simakin, A. V.; Melnik, N. N. Laser-Assisted Generation of Gold Nanoparticles and Nanostructures in Liquid and Their Plasmonic Luminescence. *Appl. Phys. A: Mater. Sci. Process.* **2014**, *115*, 747−752.

(9) Razi, S.; Madanipour, K.; Mollabashi, M. Laser Surface Texturing of 316L Stainless Steel in Air and Water: A Method for Increasing Hydrophilicity Via Direct Creation of Microstructures. *Opt. Laser Technol.* **2016**, *80*, 237−246.

(10) Zhang, D.; Gökce, B.; Sommer, S.; Streubel, R.; Barcikowski, S. Debris-Free Rear-Side Picosecond Laser Ablation of Thin Germanium Wafers in Water with Ethanol. *Appl. Surf. Sci.* **2016**, *367*, 222−230.
(11) Starinskiy, S. V.; Shukhov, Y. G.; Bulgakov, A. V. Laser-Induced Damage Thresholds of Gold, Silver and Their Alloys in Air and Water. *Appl. Surf. Sci.* **2017**, *396*, 1765−1774.
(12) Fojtik, A.; Henglein, A. Laser Ablation of Films and Suspended Particles in a Solvent - Formation of Cluster and Colloid Solutions. *Ber. Bunsenges. Phys. Chem.* **1993**, *97*, 252−254.
(13) Mafuné, F.; Kohno, J.-y.; Takeda, Y.; Kondow, T.; Sawabe, H. Formation of Gold Nanoparticles by Laser Ablation in Aqueous Solution of Surfactant. *J. Phys. Chem. B* **2001**, *105*, 5114−5120.
(14) Compagnini, G.; Scalisi, A. A.; Puglisi, O. Ablation of Noble Metals in Liquids: A Method to Obtain Nanoparticles in a Thin Polymeric Film. *Phys. Chem. Chem. Phys.* **2002**, *4*, 2787−2791.
(15) Kabashin, A. V.; Meunier, M. Synthesis of Colloidal Nanoparticles During Femtosecond Laser Ablation of Gold in Water. *J. Appl. Phys.* **2003**, *94*, 7941−7943.
(16) Sylvestre, J.-P.; Kabashin, A. V.; Sacher, E.; Meunier, M. Femtosecond Laser Ablation of Gold in Water: Influence of the Laser-Produced Plasma on the Nanoparticle Size Distribution. *Appl. Phys. A: Mater. Sci. Process.* **2005**, *80*, 753−758.
(17) Barcikowski, S.; Menendez-Manjon, A.; Chichkov, B.; Brikas, M.; Račiukaitis, G. Generation of Nanoparticle Colloids by Picosecond and Femtosecond Laser Ablations in Liquid Flow. *Appl. Phys. Lett.* **2007**, *91*, 083113.
(18) Barcikowski, S.; Devesa, F.; Moldenhauer, K. Impact and Structure of Literature on Nanoparticle Generation by Laser Ablation in Liquids. *J. Nanopart. Res.* **2009**, *11*, 1883−1893.
(19) Sylvestre, J.-P.; Kabashin, A. V.; Sacher, E.; Meunier, M.; Luong, J. H. T. Stabilization and Size Control of Gold Nanoparticles During Laser Ablation in Aqueous Cyclodextrins. *J. Am. Chem. Soc.* **2004**, *126*, 7176−7177.
(20) Dahl, J. A.; Maddux, B. L. S.; Hutchison, J. E. Toward Greener Nanosynthesis. *Chem. Rev.* **2007**, *107*, 2228−2269.
(21) Sajti, C. L.; Sattari, R.; Chichkov, B. N.; Barcikowski, S. Gram Scale Synthesis of Pure Ceramic Nanoparticles by Laser Ablation in Liquid. *J. Phys. Chem. C* **2010**, *114*, 2421−2427.
(22) Streubel, R.; Bendt, G.; Gökce, B. Pilot-Scale Synthesis of Metal Nanoparticles by High-Speed Pulsed Laser Ablation in Liquids. *Nanotechnology* **2016**, *27*, 205602.
(23) Streubel, R.; Barcikowski, S.; Gökce, B. Continuous Multigram Nanoparticle Synthesis by High-Power, High-Repetition-Rate Ultrafast Laser Ablation in Liquids. *Opt. Lett.* **2016**, *41*, 1486−1489.
(24) Morandi, V.; Marabelli, F.; Amendola, V.; Meneghetti, M.; Comoretto, D. Colloidal Photonic Crystals Doped with Gold Nanoparticles: Spectroscopy and Optical Switching Properties. *Adv. Funct. Mater.* **2007**, *17*, 2779−2786.
(25) Hess, C.; Schwenke, A.; Wagener, P.; Franzka, S.; Sajti, C.; Pflaum, M.; Wiegmann, B.; Haverich, A.; Barcikowski, S. Dose-Dependent Surface Endothelialization and Biocompatibility of Polyurethane Noble Metal Nanocomposites. *J. Biomed. Mater. Res., Part A* **2014**, *102*, 1909−1920.
(26) Petersen, S.; Barcikowski, S. In Situ Bioconjugation: Single Step Approach to Tailored Nanoparticle-Bioconjugates by Ultrashort Pulsed Laser Ablation. *Adv. Funct. Mater.* **2009**, *19*, 1167−1172.
(27) Kumar, V. L.; Siddhardha, R. S. S.; Kaniyoor, A.; Podila, R.; Molli, M.; Kumar, V. S. M.; Venkataramaniah, K.; Ramaprabhu, S.; Rao, A. M.; Ramamurthy, S. S. Gold Decorated Graphene by Laser Ablation for Efficient Electrocatalytic Oxidation of Methanol and Ethanol. *Electroanalysis* **2014**, *26*, 1850−1857.
(28) Zhang, J.; Chen, G.; Guay, D.; Chaker, M.; Ma, D. Highly Active PtAu Alloy Nanoparticle Catalysts for the Reduction of 4-Nitrophenol. *Nanoscale* **2014**, *6*, 2125−2130.
(29) Hunter, B. M.; Blakemore, J. D.; Deimund, M.; Gray, H. B.; Winkler, J. R.; Muller, A. M. Highly Active Mixed-Metal Nanosheet Water Oxidation Catalysts Made by Pulsed-Laser Ablation in Liquids. *J. Am. Chem. Soc.* **2014**, *136*, 13118−13121.
(30) Yang, G. W. Laser Ablation in Liquids: Applications in the Synthesis of Nanocrystals. *Prog. Mater. Sci.* **2007**, *52*, 648−698.
(31) Amendola, V.; Meneghetti, M. Laser Ablation Synthesis in Solution and Size Manipulation of Noble Metal Nanoparticles. *Phys. Chem. Chem. Phys.* **2009**, *11*, 3805−3821.
(32) Tarasenko, N. V.; Butsen, A. V. Laser Synthesis and Modification of Composite Nanoparticles in Liquids. *Quantum Electron.* **2010**, *40*, 986−1003.
(33) Rehbock, C.; Jakobi, J.; Gamrad, L.; van der Meer, S.; Tiedemann, D.; Taylor, U.; Kues, W.; Rath, D.; Barcikowski, S. Current State of Laser Synthesis of Metal and Alloy Nanoparticles as Ligand-Free Reference Materials for Nano-Toxicological Assays. *Beilstein J. Nanotechnol.* **2014**, *5*, 1523−1541.
(34) Asahi, T.; Mafune, F.; Rehbock, C.; Barcikowski, S. Strategies to Harvest the Unique Properties of Laser-Generated Nanomaterials in Biomedical and Energy Applications. *Appl. Surf. Sci.* **2015**, *348*, 1−3.
(35) Gorrini, F.; Cazzanelli, M.; Bazzanella, N.; Edla, R.; Gemmi, M.; Cappello, V.; David, J.; Dorigoni, C.; Bifone, A.; Miotello, A. On the Thermodynamic Path Enabling a Room-Temperature, Laser-Assisted Graphite to Nanodiamond Transformation. *Sci. Rep.* **2016**, *6*, 35244.
(36) Tarasenka, N.; Stupak, A.; Tarasenko, N.; Chakrabarti, S.; Mariotti, D. Structure and Optical Properties of Carbon Nanoparticles Generated by Laser Treatment of Graphite in Liquid. *ChemPhysChem* **2017**, *18*, 1074−1083.
(37) Tilaki, R. M.; Iraji Zad, A.; Mahdavi, S. M. Stability, Size and Optical Properties of Silver Nanoparticles Prepared by Laser Ablation in Different Carrier Media. *Appl. Phys. A: Mater. Sci. Process.* **2006**, *84*, 215−219.
(38) Bärsch, N.; Jakobi, J.; Weiler, S.; Barcikowski, S. Pure Colloidal Metal and Ceramic Nanoparticles from High-Power Picosecond Laser Ablation in Water and Acetone. *Nanotechnology* **2009**, *20*, 445603.
(39) Musaev, O. R.; Driver, M. S.; Sutter, E. A.; Caruso, A. N.; Wrobel, J. M.; Kruger, M. B. Influence of the Liquid Environment on the Products Formed from the Laser Ablation of Tin. *Appl. Phys. A: Mater. Sci. Process.* **2013**, *113*, 355−359.
(40) Jung, H. J.; Choi, M. Y. Specific Solvent Produces Specific Phase Ni Nanoparticles: A Pulsed Laser Ablation in Solvents. *J. Phys. Chem. C* **2014**, *118*, 14647−14654.
(41) Muñetón Arboleda, D.; Santillán, J. M. J.; Mendoza Herrera, L. J.; van Raap, M. B. F.; Zélis, P. M.; Muraca, D.; Schinca, D. C.; Scaffardi, L. B. Synthesis of Ni Nanoparticles by Femtosecond Laser Ablation in Liquids: Structure and Sizing. *J. Phys. Chem. C* **2015**, *119*, 13184−13193.
(42) Gökce, B.; van't Zand, D. D.; Menéndez-Manjón, A.; Barcikowski, S. Ripening Kinetics of Laser-Generated Plasmonic Nanoparticles in Different Solvents. *Chem. Phys. Lett.* **2015**, *626*, 96−101.
(43) Lasemi, N.; Pacher, U.; Rentenberger, C.; Bomati-Miguel, O.; Kautek, W. Laser-Assisted Synthesis of Colloidal Ni-Core/NiO_x-Shell Nanoparticles in Water and Alcoholic Solvents. *ChemPhysChem* **2017**, *18*, 1118−1124.
(44) Kanitz, A.; Hoppius, J. S.; Del Mar Sanz, M.; Maicas, M.; Ostendorf, A.; Gurevich, E. L. Synthesis of Magnetic Nanoparticles by Ultrashort Pulsed Laser Ablation of Iron in Different Liquids. *ChemPhysChem* **2017**, *18*, 1155−1164.
(45) Soliman, W.; Takada, N.; Sasaki, K. Effect of Water Pressure on Size of Nanoparticles in Liquid-Phase Laser Ablation. *Jpn. J. Appl. Phys.* **2011**, *50*, 108003.
(46) De Giacomo, A.; De Bonis, A.; Dell'Aglio, M.; De Pascale, O.; Gaudiuso, R.; Orlando, S.; Santagata, A.; Senesi, G. S.; Taccogna, F.; Teghil, R. Laser Ablation of Graphite in Water in a Range of Pressure from 1 to 146 atm Using Single and Double Pulse Techniques for the Production of Carbon Nanostructures. *J. Phys. Chem. C* **2011**, *115*, 5123−5130.
(47) Menéndez-Manjón, A.; Chichkov, B.; Barcikowski, S. Influence of Water Temperature on the Hydrodynamic Diameter of Gold Nanoparticles from Laser Ablation. *J. Phys. Chem. C* **2010**, *114*, 2499−2504.

DOI: 10.1021/acs.jpcc.7b02301
J. Phys. Chem. C 2017, 121, 16549−16567

(48) Compagnini, G.; Scalisi, A. A.; Puglisi, O.; Spinella, C. Synthesis of Gold Colloids by Laser Ablation in Thiol-Alkane Solutions. *J. Mater. Res.* **2004**, *19*, 2795−2798.
(49) Tsuji, T.; Thang, D.-H.; Okazaki, Y.; Nakanishi, M.; Tsuboi, Y.; Tsuji, M. Preparation of Silver Nanoparticles by Laser Ablation in Polyvinylpyrrolidone Solutions. *Appl. Surf. Sci.* **2008**, *254*, 5224−5230.
(50) Rehbock, C.; Merk, V.; Gamrad, L.; Streubel, R.; Barcikowski, S. Size Control of Laser-Fabricated Surfactant-Free Gold Nanoparticles with Highly Diluted Electrolytes and Their Subsequent Bioconjugation. *Phys. Chem. Chem. Phys.* **2013**, *15*, 3057−3067.
(51) Amendola, V.; Meneghetti, M. Controlled Size Manipulation of Free Gold Nanoparticles by Laser Irradiation and Their Facile Bioconjugation. *J. Mater. Chem.* **2007**, *17*, 4705−4710.
(52) Besner, S.; Kabashin, A. V.; Winnik, F. M.; Meunier, M. Synthesis of Size-Tunable Polymer-Protected Gold Nanoparticles by Femtosecond Laser-Based Ablation and Seed Growth. *J. Phys. Chem. C* **2009**, *113*, 9526−9531.
(53) Wang, H. Q.; Pyatenko, A.; Kawaguchi, K.; Li, X.; Swiatkowska-Warkocka, Z.; Koshizaki, N. Selective Pulsed Heating for the Synthesis of Semiconductor and Metal Submicrometer Spheres. *Angew. Chem., Int. Ed.* **2010**, *49*, 6361−6364.
(54) Hashimoto, S.; Werner, D.; Uwada, T. Studies on the Interaction of Pulsed Lasers with Plasmonic Gold Nanoparticles toward Light Manipulation, Heat Management, and Nanofabrication. *J. Photochem. Photobiol., C* **2012**, *13*, 28−54.
(55) Yan, Z. J.; Bao, R. G.; Huang, Y.; Chrisey, D. B. Hollow Particles Formed on Laser-Induced Bubbles by Excimer Laser Ablation of Al in Liquid. *J. Phys. Chem. C* **2010**, *114*, 11370−11374.
(56) Niu, K. Y.; Yang, J.; Kulinich, S. A.; Sun, J.; Li, H.; Du, X. W. Morphology Control of Nanostructures Via Surface Reaction of Metal Nanodroplets. *J. Am. Chem. Soc.* **2010**, *132*, 9814−9819.
(57) Zhang, D.; Gökce, B.; Notthoff, C.; Barcikowski, S. Layered Seed-Growth of AgGe Football-Like Microspheres via Precursor-Free Picosecond Laser Synthesis in Water. *Sci. Rep.* **2015**, *5*, 13661.
(58) Zhang, D.; Gökce, B.; Barcikowski, S. Laser Synthesis and Processing of Colloids: Fundamentals and Applications. *Chem. Rev.* **2017**, *117*, 3990−4103.
(59) Xiao, J.; Liu, P.; Wang, C. X.; Yang, G. W. External Field-Assisted Laser Ablation in Liquid: An Efficient Strategy for Nanocrystal Synthesis and Nanostructure Assembly. *Prog. Mater. Sci.* **2017**, *87*, 140−220.
(60) Tamura, A.; Sakka, T.; Fukami, K.; Ogata, Y. H. Dynamics of Cavitation Bubbles Generated by Multi-Pulse Laser Irradiation of a Solid Target in Water. *Appl. Phys. A: Mater. Sci. Process.* **2013**, *112*, 209−213.
(61) Dell'Aglio, M.; Gaudiuso, R.; De Pascale, O.; De Giacomo, A. Mechanisms and Processes of Pulsed Laser Ablation in Liquids During Nanoparticle Production. *Appl. Surf. Sci.* **2015**, *348*, 4−9.
(62) Lam, J.; Lombard, J.; Dujardin, C.; Ledoux, G.; Merabia, S.; Amans, D. Dynamical Study of Bubble Expansion Following Laser Ablation in Liquids. *Appl. Phys. Lett.* **2016**, *108*, 074104.
(63) Ibrahimkutty, S.; Wagener, P.; Menzel, A.; Plech, A.; Barcikowski, S. Nanoparticle Formation in a Cavitation Bubble after Pulsed Laser Ablation in Liquid Studied with High Time Resolution Small Angle X-Ray Scattering. *Appl. Phys. Lett.* **2012**, *101*, 103104.
(64) Wagener, P.; Ibrahimkutty, S.; Menzel, A.; Plech, A.; Barcikowski, S. Dynamics of Silver Nanoparticle Formation and Agglomeration inside the Cavitation Bubble after Pulsed Laser Ablation in Liquid. *Phys. Chem. Chem. Phys.* **2013**, *15*, 3068−3074.
(65) Ibrahimkutty, S.; Wagener, P.; Rolo, T. D.; Karpov, D.; Menzel, A.; Baumbach, T.; Barcikowski, S.; Plech, A. A Hierarchical View on Material Formation During Pulsed-Laser Synthesis of Nanoparticles in Liquid. *Sci. Rep.* **2015**, *5*, 16313.
(66) Letzel, A.; Gökce, B.; Wagener, P.; Ibrahimkutty, S.; Menzel, A.; Plech, A.; Barcikowski, S. Size Quenching During Laser Synthesis of Colloids Happens Already in the Vapor Phase of the Cavitation Bubble. *J. Phys. Chem. C* **2017**, *121*, 5356−5365.
(67) Povarnitsyn, M. E.; Itina, T. E.; Levashov, P. R.; Khishchenko, K. V. Mechanisms of Nanoparticle Formation by Ultra-Short Laser Ablation of Metals in Liquid Environment. *Phys. Chem. Chem. Phys.* **2013**, *15*, 3108−3114.
(68) Povarnitsyn, M. E.; Itina, T. E. Hydrodynamic Modeling of Femtosecond Laser Ablation of Metals in Vacuum and in Liquid. *Appl. Phys. A: Mater. Sci. Process.* **2014**, *117*, 175−178.
(69) Zhigilei, L. V.; Lin, Z.; Ivanov, D. S.; Leveugle, E.; Duff, W. H.; Thomas, D.; Sevilla, C.; Guy, S. J. Atomic/Molecular-Level Simulations of Laser-Materials Interactions. In *Laser-Surface Interactions for New Materials Production: Tailoring Structure and Properties*, Springer Series in Materials Science; Miotello, A., Ossi, P. M., Eds.; Springer-Verlag Berlin Heidelberg: Berlin, 2010; Vol. *130*, pp 43−79.
(70) Wu, C.; Karim, E. T.; Volkov, A. N.; Zhigilei, L. V. *Atomic Movies of Laser-Induced Structural and Phase Transformations from Molecular Dynamics Simulations, in Lasers in Materials Science*, Springer Series in Materials Science; Castillejo, M., Ossi, P. M., Zhigilei, L. V., Eds.; Springer International Publishing: Switzerland, 2014; Vol. *191*, pp 67−100.
(71) Shugaev, M. V.; Wu, C.; Armbruster, O.; Naghilou, A.; Brouwer, N.; Ivanov, D. S.; Derrien, T. J. Y.; Bulgakova, N. M.; Kautek, W.; Rethfeld, B.; Zhigilei, L. V. Fundamentals of Ultrafast Laser-Material Interaction. *MRS Bull.* **2016**, *41*, 960−968.
(72) Tabetah, M.; Matei, A.; Constantinescu, C.; Mortensen, N. P.; Dinescu, M.; Schou, J.; Zhigilei, L. V. The Minimum Amount of "Matrix" Needed for Matrix-Assisted Pulsed Laser Deposition of Biomolecules. *J. Phys. Chem. B* **2014**, *118*, 13290−13299.
(73) Zou, J.; Wu, C.; Robertson, W. D.; Zhigilei, L. V.; Miller, R. J. D. Molecular Dynamics Investigation of Desorption and Ion Separation Following Picosecond Infrared Laser (PIRL) Ablation of an Ionic Aqueous Protein Solution. *J. Chem. Phys.* **2016**, *145*, 204202.
(74) Shih, C.-Y.; Wu, C.; Shugaev, M. V.; Zhigilei, L. V. Atomistic Modeling of Nanoparticle Generation in Short Pulse Laser Ablation of Thin Metal Films in Water. *J. Colloid Interface Sci.* **2017**, *489*, 3−17.
(75) Karim, E. T.; Shugaev, M. V.; Wu, C.; Lin, Z.; Hainsey, R. F.; Zhigilei, L. V. Atomistic Simulation Study of Short Pulse Laser Interactions with a Metal Target under Conditions of Spatial Confinement by a Transparent Overlayer. *J. Appl. Phys.* **2014**, *115*, 183501.
(76) Shugaev, M. V.; Shih, C.-Y.; Karim, E. T.; Wu, C.; Zhigilei, L. V. Generation of Nanocrystalline Surface Layer in Short Pulse Laser Processing of Metal Targets under Conditions of Spatial Confinement by Solid or Liquid Overlayer. *Appl. Surf. Sci.* **2017**, *417*, 54−63.
(77) Ivanov, D. S.; Zhigilei, L. V. Combined Atomistic-Continuum Modeling of Short-Pulse Laser Melting and Disintegration of Metal Films. *Phys. Rev. B: Condens. Matter Mater. Phys.* **2003**, *68*, 064114.
(78) Zhigilei, L. V.; Lin, Z.; Ivanov, D. S. Atomistic Modeling of Short Pulse Laser Ablation of Metals: Connections between Melting, Spallation, and Phase Explosion. *J. Phys. Chem. C* **2009**, *113*, 11892−11906.
(79) Wu, C.; Zhigilei, L. V. Microscopic Mechanisms of Laser Spallation and Ablation of Metal Targets from Large-Scale Molecular Dynamics Simulations. *Appl. Phys. A: Mater. Sci. Process.* **2014**, *114*, 11−32.
(80) Wu, C.; Christensen, M. S.; Savolainen, J.-M.; Balling, P.; Zhigilei, L. V. Generation of Subsurface Voids and a Nanocrystalline Surface Layer in Femtosecond Laser Irradiation of a Single-Crystal Ag Target. *Phys. Rev. B: Condens. Matter Mater. Phys.* **2015**, *91*, 035413.
(81) Wu, C.; Zhigilei, L. V. Nanocrystalline and Polyicosahedral Structure of a Nanospike Generated on Metal Surface Irradiated by a Single Femtosecond Laser Pulse. *J. Phys. Chem. C* **2016**, *120*, 4438−4447.
(82) Anisimov, S. I.; Kapeliovich, B. L.; Perel'man, T. L. Electron Emission from Metal Surfaces Exposed to Ultrashort Laser Pulses. *Sov. Phys. JETP* **1974**, *39*, 375−377.
(83) Wellershoff, S.-S.; Hohlfeld, J.; Güdde, J.; Matthias, E. The Role of Electron-Phonon Coupling in Femtosecond Laser Damage of Metals. *Appl. Phys. A: Mater. Sci. Process.* **1999**, *69*, S99−S107.
(84) Byskov-Nielsen, J.; Savolainen, J.-M.; Christensen, M. S.; Balling, P. Ultra-Short Pulse Laser Ablation of Copper, Silver and

DOI: 10.1021/acs.jpcc.7b02301
J. Phys. Chem. C 2017, 121, 16549−16567

Tungsten: Experimental Data and Two-Temperature Model Simulations. *Appl. Phys. A: Mater. Sci. Process.* **2011**, *103*, 447−453.
(85) Levy, Y.; Derrien, T. J.-Y.; Bulgakova, N. M.; Gurevich, E. L.; Mocek, T. Relaxation Dynamics of Femtosecond-Laser-Induced Temperature Modulation on the Surfaces of Metals and Semiconductors. *Appl. Surf. Sci.* **2016**, *374*, 157−164.
(86) Ivanov, D. S.; Zhigilei, L. V. Combined Atomistic-Continuum Model for Simulation of Laser Interaction with Metals: Application in the Calculation of Melting Thresholds in Ni Targets of Varying Thickness. *Appl. Phys. A: Mater. Sci. Process.* **2004**, *79*, 977−981.
(87) Ivanov, D. S.; Rethfeld, B.; O'Connor, G. M.; Glynn, T. J.; Volkov, A. N.; Zhigilei, L. V. The Mechanism of Nanobump Formation in Femtosecond Pulse Laser Nanostructuring of Thin Metal Films. *Appl. Phys. A: Mater. Sci. Process.* **2008**, *92*, 791−796.
(88) Ivanov, D. S.; Lin, Z.; Rethfeld, B.; O'Connor, G. M.; Glynn, T. J.; Zhigilei, L. V. Nanocrystalline Structure of Nanobump Generated by Localized Photo-Excitation of Metal Film. *J. Appl. Phys.* **2010**, *107*, 013519.
(89) Ivanov, D. S.; Lipp, V. P.; Blumenstein, A.; Kleinwort, F.; Veiko, V. P.; Yakovlev, E.; Roddatis, V.; Garcia, M. E.; Rethfeld, B.; Ihlemann, J.; Simon, P. Experimental and Theoretical Investigation of Periodic Nanostructuring of Au with Ultrashort UV Laser Pulses near the Damage Threshold. *Phys. Rev. Appl.* **2015**, *4*, 064006.
(90) Zhigilei, L. V.; Garrison, B. J. Pressure Waves in Microscopic Simulations of Laser Ablation. *MRS Online Proc. Libr.* **1999**, *538*, 491−496.
(91) Schäfer, C.; Urbassek, H. M.; Zhigilei, L. V.; Garrison, B. J. Pressure-Transmitting Boundary Conditions for Molecular-Dynamics Simulations. *Comput. Mater. Sci.* **2002**, *24*, 421−429.
(92) Zhigilei, L. V.; Ivanov, D. S. Channels of Energy Redistribution in Short-Pulse Laser Interactions with Metal Targets. *Appl. Surf. Sci.* **2005**, *248*, 433−439.
(93) Foiles, S. M.; Baskes, M. I.; Daw, M. S. Embedded-Atom-Method Functions for the FCC Metals Cu, Ag, Au, Ni, Pd, Pt, and Their Alloys. *Phys. Rev. B: Condens. Matter Mater. Phys.* **1986**, *33*, 7983−7991.
(94) Voter, A. F.; Chen, S. P. Accurate Interatomic Potentials for Ni, Al, and Ni_3Al. *MRS Online Proc. Libr.* **1986**, *82*, 175−180.
(95) Foiles, S. M.; Adams, J. B. Thermodynamic Properties of FCC Transition Metals as Calculated with the Embedded-Atom Method. *Phys. Rev. B: Condens. Matter Mater. Phys.* **1989**, *40*, 5909−5915.
(96) Wu, C.; Thomas, D. A.; Lin, Z.; Zhigilei, L. V. Runaway Lattice-Mismatched Interface in an Atomistic Simulation of Femtosecond Laser Irradiation of Ag Film-Cu Substrate System. *Appl. Phys. A: Mater. Sci. Process.* **2011**, *104*, 781−792.
(97) Haynes, W. M. *CRC Handbook of Chemistry and Physics*, 97th ed.; CRC Press: Boca Raton, FL, 2016.
(98) Garrison, B. J.; Itina, T. E.; Zhigilei, L. V. Limit of Overheating and the Threshold Behavior in Laser Ablation. *Phys. Rev. E* **2003**, *68*, 041501.
(99) Miotello, A.; Kelly, R. Laser-Induced Phase Explosion: New Physical Problems When a Condensed Phase Approaches the Thermodynamic Critical Temperature. *Appl. Phys. A: Mater. Sci. Process.* **1999**, *69*, S67−S73.
(100) Bulgakova, N. M.; Bulgakov, A. V. Pulsed Laser Ablation of Solids: Transition from Normal Vaporization to Phase Explosion. *Appl. Phys. A: Mater. Sci. Process.* **2001**, *73*, 199−208.
(101) Ohse, R. W.; von Tippelskirch, H. The Critical Constants of the Elements and of Some Refractory Materials with High Critical Temperatures. (A Review). *High Temp-High Press* **1977**, *9*, 367−385.
(102) Lin, Z.; Zhigilei, L. V.; Celli, V. Electron-Phonon Coupling and Electron Heat Capacity of Metals under Conditions of Strong Electron-Phonon Nonequilibrium. *Phys. Rev. B: Condens. Matter Mater. Phys.* **2008**, *77*, 075133.
(103) Groeneveld, R. H. M.; Sprik, R.; Lagendijk, A. Femtosecond Spectroscopy of Electron-Electron and Electron-Phonon Energy Relaxation in Ag and Au. *Phys. Rev. B: Condens. Matter Mater. Phys.* **1995**, *51*, 11433−11445.
(104) Mills, K. C.; Monaghan, B. J.; Keene, B. J. Thermal Conductivities of Molten Metals: Part 1 Pure Metals. *Int. Mater. Rev.* **1996**, *41*, 209−242.
(105) Zhigilei, L. V.; Kodali, P. B. S.; Garrison, B. J. Molecular Dynamics Model for Laser Ablation and Desorption of Organic Solids. *J. Phys. Chem. B* **1997**, *101*, 2028−2037.
(106) Zhigilei, L. V.; Leveugle, E.; Garrison, B. J.; Yingling, Y. G.; Zeifman, M. I. Computer Simulations of Laser Ablation of Molecular Substrates. *Chem. Rev.* **2003**, *103*, 321−347.
(107) Phares, D. J.; Srinivasa, A. R. Molecular Dynamics with Molecular Temperature. *J. Phys. Chem. A* **2004**, *108*, 6100−6108.
(108) Jacobs, W. M.; Nicholson, D. A.; Zemer, H.; Volkov, A. N.; Zhigilei, L. V. Acoustic Energy Dissipation and Thermalization in Carbon Nanotubes: Atomistic Modeling and Mesoscopic Description. *Phys. Rev. B: Condens. Matter Mater. Phys.* **2012**, *86*, 165414.
(109) Michaelides, A.; Ranea, V. A.; de Andres, P. L.; King, D. A. General Model for Water Monomer Adsorption on Close-Packed Transition and Noble Metal Surfaces. *Phys. Rev. Lett.* **2003**, *90*, 216102.
(110) Ren, J.; Meng, S. First-Principles Study of Water on Copper and Noble Metal (110) Surfaces. *Phys. Rev. B: Condens. Matter Mater. Phys.* **2008**, *77*, 054110.
(111) Hughes, Z. E.; Wright, L. B.; Walsh, T. R. Biomolecular Adsorption at Aqueous Silver Interfaces: First-Principles Calculations, Polarizable Force-Field Simulations, and Comparisons with Gold. *Langmuir* **2013**, *29*, 13217−13229.
(112) Michaelides, A.; Alavi, A.; King, D. A. Insight into H_2O-Ice Adsorption and Dissociation on Metal Surfaces from First-Principles Simulations. *Phys. Rev. B: Condens. Matter Mater. Phys.* **2004**, *69*, 113404.
(113) Yingling, Y. G.; Zhigilei, L. V.; Garrison, B. J. Photochemical Fragmentation Processes in Laser Ablation of Organic Solids. *Nucl. Instrum. Methods Phys. Res., Sect. B* **2001**, *180*, 171−175.
(114) Yingling, Y. G.; Zhigilei, L. V.; Garrison, B. J. The Role of the Photochemical Fragmentation in Laser Ablation: A Molecular Dynamics Study. *J. Photochem. Photobiol., A* **2001**, *145*, 173−181.
(115) Bäuerle, D. *Laser Processing and Chemistry*; Springer-Verlag: Berlin Heidelberg, 2000.
(116) Kunze, H. J. *Introduction to Plasma Spectroscopy*; Springer-Verlag: Berlin Heidelberg, 2009.
(117) Griem, H. R. High-Density Corrections in Plasma Spectroscopy. *Phys. Rev.* **1962**, *128*, 997−1003.
(118) Taccogna, F. Nucleation and Growth of Nanoparticles in a Plasma by Laser Ablation in Liquid. *J. Plasma Phys.* **2015**, *81*, 495810509.
(119) Paltauf, G.; Dyer, P. E. Photomechanical Processes and Effects in Ablation. *Chem. Rev.* **2003**, *103*, 487−518.
(120) Leveugle, E.; Ivanov, D. S.; Zhigilei, L. V. Photomechanical Spallation of Molecular and Metal Targets: Molecular Dynamics Study. *Appl. Phys. A: Mater. Sci. Process.* **2004**, *79*, 1643−1655.
(121) Demaske, B. J.; Zhakhovsky, V. V.; Inogamov, N. A.; Oleynik, I. I. Ablation and Spallation of Gold Films Irradiated by Ultrashort Laser Pulses. *Phys. Rev. B: Condens. Matter Mater. Phys.* **2010**, *82*, 064113.
(122) Savolainen, J.-M.; Christensen, M. S.; Balling, P. Material Swelling as the First Step in the Ablation of Metals by Ultrashort Laser Pulses. *Phys. Rev. B: Condens. Matter Mater. Phys.* **2011**, *84*, 193410.
(123) Ionin, A. A.; Kudryashov, S. I.; Ligachev, A. E.; Makarov, S. V.; Seleznev, L. V.; Sinitsyn, D. V. Nanoscale Cavitation Instability of the Surface Melt Along the Grooves of One-Dimensional Nanorelief Gratings on an Aluminum Surface. *JETP Lett.* **2011**, *94*, 266−269.
(124) Ashitkov, S. I.; Inogamov, N. A.; Zhakhovskii, V. V.; Emirov, Y. N.; Agranat, M. B.; Oleinik, I. I.; Anisimov, S. I.; Fortov, V. E. Formation of Nanocavities in the Surface Layer of an Aluminum Target Irradiated by a Femtosecond Laser Pulse. *JETP Lett.* **2012**, *95*, 176−181.
(125) Starikov, S. V.; Pisarev, V. V. Atomistic Simulation of Laser-Pulse Surface Modification: Predictions of Models with Various Length and Time Scales. *J. Appl. Phys.* **2015**, *117*, 135901.

DOI: 10.1021/acs.jpcc.7b02301
J. Phys. Chem. C 2017, 121, 16549−16567

(126) Zhigilei, L. V. Dynamics of the Plume Formation and Parameters of the Ejected Clusters in Short-Pulse Laser Ablation. *Appl. Phys. A: Mater. Sci. Process.* **2003**, *76*, 339−350.
(127) http://www.factsage.com/.
(128) Rouleau, C. M.; Shih, C.-Y.; Wu, C.; Zhigilei, L. V.; Puretzky, A. A.; Geohegan, D. B. Nanoparticle Generation and Transport Resulting from Femtosecond Laser Ablation of Ultrathin Metal Films: Time-Resolved Measurements and Molecular Dynamics Simulations. *Appl. Phys. Lett.* **2014**, *104*, 193106.
(129) Vrij, A. Possible Mechanism for the Spontaneous Rupture of Thin, Free Liquid Films. *Discuss. Faraday Soc.* **1966**, *42*, 23−33.
(130) Kull, H. J. Theory of the Rayleigh-Taylor Instability. *Phys. Rep.* **1991**, *206*, 197−325.
(131) Chandrasekhar, S. *Hydrodynamic and Hydromagnetic Stability*; Oxford University Press: Oxford, 1961.
(132) Gloor, G. J.; Jackson, G.; Blas, F. J.; de Miguel, E. Test-Area Simulation Method for the Direct Determination of the Interfacial Tension of Systems with Continuous or Discontinuous Potentials. *J. Chem. Phys.* **2005**, *123*, 134703.
(133) Kadau, K.; Germann, T. C.; Hadjiconstantinou, N. G.; Lomdahl, P. S.; Dimonte, G.; Holian, B. L.; Alder, B. J. Nanohydrodynamics Simulations: An Atomistic View of the Rayleigh-Taylor Instability. *Proc. Natl. Acad. Sci. U. S. A.* **2004**, *101*, 5851−5855.
(134) Barber, J. L.; Kadau, K.; Germann, T. C.; Alder, B. J. Initial Growth of the Rayleigh-Taylor Instability via Molecular Dynamics. *Eur. Phys. J. B* **2008**, *64*, 271−276.
(135) Kirkwood, S. E.; van Popta, A. C.; Tsui, Y. Y.; Fedosejevs, R. Single and Multiple Shot near-Infrared Femtosecond Laser Pulse Ablation Thresholds of Copper. *Appl. Phys. A: Mater. Sci. Process.* **2005**, *81*, 729−735.
(136) Krüger, J.; Dufft, D.; Koter, R.; Hertwig, A. Femtosecond Laser-Induced Damage of Gold Films. *Appl. Surf. Sci.* **2007**, *253*, 7815−7819.
(137) Raciukaitis, G.; Brikas, M.; Gecys, P.; Gedvilas, M.; Phipps, C. R. Accumulation Effects in Laser Ablation of Metals with High-Repetition-Rate Lasers. *Proc. SPIE* **2008**, *7005*, 70052L.
(138) Byskov-Nielsen, J.; Savolainen, J.-M.; Christensen, M. S.; Balling, P. Ultra-Short Pulse Laser Ablation of Metals: Threshold Fluence, Incubation Coefficient and Ablation Rates. *Appl. Phys. A: Mater. Sci. Process.* **2010**, *101*, 97−101.
(139) Armbruster, O.; Naghilou, A.; Kitzler, M.; Kautek, W. Spot Size and Pulse Number Dependence of Femtosecond Laser Ablation Thresholds of Silicon and Stainless Steel. *Appl. Surf. Sci.* **2017**, *396*, 1736−1740.
(140) Brouillette, M. The Richtmyer-Meshkov Instability. *Annu. Rev. Fluid Mech.* **2002**, *34*, 445−468.
(141) Mikaelian, K. O. Richtmyer-Meshkov Instability of Arbitrary Shapes. *Phys. Fluids* **2005**, *17*, 034101.
(142) Buttler, W. T.; Oró, D. M.; Preston, D. L.; Mikaelian, K. O.; Cherne, F. J.; Hixson, R. S.; Mariam, F. G.; Morris, C.; Stone, J. B.; Terrones, G.; Tupa, D. Unstable Richtmyer-Meshkov Growth of Solid and Liquid Metals in Vacuum. *J. Fluid Mech.* **2012**, *703*, 60−84.
(143) Durand, O.; Soulard, L. Power Law and Exponential Ejecta Size Distributions from the Dynamic Fragmentation of Shock-Loaded Cu and Sn Metals under Melt Conditions. *J. Appl. Phys.* **2013**, *114*, 194902.
(144) Dimonte, G.; Terrones, G.; Cherne, F. J.; Ramaprabhu, P. Ejecta Source Model Based on the Nonlinear Richtmyer-Meshkov Instability. *J. Appl. Phys.* **2013**, *113*, 024905.
(145) Dyachkov, S.; Parshikov, A.; Zhakhovsky, V. Ejecta from Shocked Metals: Comparative Simulations Using Molecular Dynamics and Smoothed Particle Hydrodynamics. *AIP Conf. Proc.* **2017**, *1793*, 100024.
(146) Eggers, J.; Villermaux, E. Physics of Liquid Jets. *Rep. Prog. Phys.* **2008**, *71*, 036601.
(147) Moseler, M.; Landman, U. Formation, Stability, and Breakup of Nanojets. *Science* **2000**, *289*, 1165−1169.
(148) Santillán, J. M. J.; Fernández van Raap, M. B.; Mendoza Zélis, P.; Coral, D.; Muraca, D.; Schinca, D. C.; Scaffardi, L. B. Ag Nanoparticles Formed by Femtosecond Pulse Laser Ablation in Water: Self-Assembled Fractal Structures. *J. Nanopart. Res.* **2015**, *17*, 86.
(149) Merabia, S.; Shenogin, S.; Joly, L.; Keblinski, P.; Barrat, J.-L. Heat Transfer from Nanoparticles: A Corresponding State Analysis. *Proc. Natl. Acad. Sci. U. S. A.* **2009**, *106*, 15113−15118.
(150) Merabia, S.; Keblinski, P.; Joly, L.; Lewis, L. J.; Barrat, J. L. Critical Heat Flux Around Strongly Heated Nanoparticles. *Phys. Rev. E* **2009**, *79*, 021404.
(151) Hu, M.; Poulikakos, D.; Grigoropoulos, C. P.; Pan, H. Recrystallization of Picosecond Laser-Melted ZnO Nanoparticles in a Liquid: A Molecular Dynamics Study. *J. Chem. Phys.* **2010**, *132*, 164504.
(152) Deng, C.; Sansoz, F. Fundamental Differences in the Plasticity of Periodically Twinned Nanowires in Au, Ag, Al, Cu, Pb and Ni. *Acta Mater.* **2009**, *57*, 6090−6101.

DOI: 10.1021/acs.jpcc.7b02301
J. Phys. Chem. C 2017, 121, 16549−16567